2008

Operation And Improvement Of The Iwrap Airborne Doppler Radar/Scatterometer

Tao Chu
University of Massachusetts Amherst

OPERATION AND IMPROVEMENT OF THE IWRAP AIRBORNE DOPPLER RADAR/SCATTEROMETER

A Thesis Presented

by

TAO CHU

Submitted to the Graduate School of the
University of Massachusetts Amherst in partial fulfillment
of the requirements for the degree of

MASTER OF SCIENCE IN ELECTRICAL AND COMPUTER ENGINEERING

February 2008

Electrical and Computer Engineering

OPERATION AND IMPROVEMENT OF THE IWRAP AIRBORNE DOPPLER RADAR/SCATTEROMETER

A Thesis Presented

by

TAO CHU

Approved as to style and content by:

Stephen J. Frasier, Chair

Paul Siqueira, Member

Daniel H. Schaubert, Member

Christopher V. Hollot, Department Chair
Electrical and Computer Engineering

To my mother and father for the struggles they have gone through in their lives.

ACKNOWLEDGMENTS

There are those few people you meet in life with whom you do not share any previous connection with, but who can inadvertently and unexpectedly carry out drastic good deeds to alter the course of one's life. Without Steve Sekelsky, I would not have been introduced to the field of Microwave Remote Sensing, got to know MIRSL, and taken an interest in graduate school in this great program. Thank you for being the catalyst to the changes undertaken during a critical period of my life.

I would like to thank my academic adviser Stephen Frasier for accepting me as a graduate student at MIRSL, and putting me on the IWRAP project to fly in a 70's research airplane that deliberately goes into hurricanes. Because of IWRAP, I was able to travel and see the world. Thank you for introducing me to the exciting scientific community, and to the personal and the professional connections I will forever treasure. My time at MIRSL has taught me to be patient, methodical, and gave me vision to see a bridge between scientific theory and the real world.

I was told once at MIRSL the instruments built come and go, the only things left are the published papers. Students at MIRSL also come and go, and the only things left are the memories and the friendships among isolated individuals. However I believe they are the very core of the lab reputation and heartbeat. It has been great being part of the MIRSL family. Special thanks to MIRSL graduates: Harry Figueroa, for being there for me when I first entered MIRSL; Kery Hardwick, the cool hippy; Mario Behn, the guy who was constantly complaining about something, but I loved listening to it; Peter Asuzu, who had helped me so much to get me started on IWRAP and had sacrificed so much. I would also like to thank the friendly combatants, the current Les Miserables: the Jorges, Gita, Yonghong, Brian, Tony, Razi, Pei,

and my buddies Joe and Harish or HVHV. Finally I want to thank my Serbian mom and Croatian dad: Dragana Perkovic, without you, MIRSL will crumble into pieces. Thank you for always being thorough whenever you are helping me. Ninoslav Majurec, you are my greatest mentor and teacher. Thank you for your patience and all the conversations. I can not imagine my experience at MIRSL without you.

I would like to also acknowledge my mentors outside of MIRSL for their support and guidance, especially during the field campaigns. Paul Chang, thanks for taking me under your wing during the field experiments; Zorana Jelenak, you are the great pillar of NOAA/NESDIS, I look forward to work with you; and Jim Carswell, your expertise in the subject and your methodicalness have always amazed me, thanks for all the ideas and help in clutch situations. My gratitude goes to the NOAA/AOC personnel, especially Sean McMillan, you are the funniest man I have met and an exemplary family man, Bobby Peek for your help, and Jim McFadden for your professionalism.

Daniel Esteban Fernandez, the guy with the two last names, thank you for passing onto me the knowledge about IWRAP. You have taught me so much more than that. I will remember you best for being stopped at the bar because of your hole-punched Massachusetts driver's license then being hunted for your Spanish passport, the glacier climbing, the curling games, the single malt tasting session, the oyster and salmon dinner at Elliotts, the calamari at Orso, the Pinot Noir in St. Johns, and most importantly, the times at that base on Dale Mabry. Thank you for being my mentor of life and a friend.

I would like to mention my old friends JJ, James, Scott, and Karen, although you are far away, you have been my emotional lift during this journey. I am extremely thankful for the new friends that I have made during my graduate experience at UMass. My brothers and sisters: Cai Yan, Tang Wen, Huang Yong, Sun Jie, for looking out for me and getting me in touch with my roots. I also would like to

mention my friends in Prince Hall for they have brought me joy in a tough stretch, special people in a special place: Hellen, Jose, Danai, Ahbinev, Chen Xi, Linda, Joleen, and Hao Jing.

Thanks goes to my family for the support they provided me throughout this journey. Lily, I hope I am setting a good example for you. Let me know if I'm not, I'll fix it. To my brother Shaohan, my step father; my sister Li Yang, my step mother. I think people and relationship are both malleable, future is filled with optimism. To my father, this work is dedicated to you because I want to show you that I can. I hope I have not been too much of a disappointment and I hope we can make up the times we have lost. Finally, I want to thank my mother for giving me this new life full of adventures, but also for leaving me with the imagination for the road not taken. Anything positive I accomplish during my life time will always have your fingerprints all over it, thank you for your support and understanding. This work is dedicated to you.

TABLE OF CONTENTS

LIST OF TABLES

Table **Page**

LIST OF FIGURES

Figure **Page**

CHAPTER 1

INTRODUCTION

1.1 Scientific Motivation

Radar scatterometry offers valuable ocean surface vector wind (OSVW) products, which enable forecasting, nowcasting, and improvement of the understanding of the inner structure of severe weather events such as tropical cyclones [1]. Satellite-based scatterometers observe the Earth's surface from polar orbits at 800 km altitude. They provide good global coverage but have limited spatial resolution, providing limited information inside tropical cyclones [8].

Scatterometers were first introduced during World War II and have been used extensively for both land-based and airborne measurements since then. The first scatterometer in space was the S-193 RADSCAT flown on Skylab in 1974 which collected large amount of data during its operation in 1973 and 1974. The measurements revealed that the ocean backscatter was correlated with the wind speed and suggested a power law relationship for incidence angles ranging from 30 to 50 degrees. Since then, several spaceborne scatterometers have obtained backscatter measurements including SASS and ERS-1,2. The NASA scatterometer NSCAT was launched on board the Japanese satellite ADEOS1 in August 1996. After 10 month of operation, the satellite suffered a catastrophic power failure. NASA immediately approved a replacement of the NSCAT mission identical to Seawind on board QuikSCAT satellite. The QuikSCAT mission was launched in 1999 and was developed to provide daily OSVW over the oceans using a spaceborne Ku-band scatterometer at 13.4 GHz. The Seawind scatterometer was designed as a conically scanning, dual-beam scatterom-

eter system. It has an orbital swath of 1800 km which nearly covers 90 percent of earth surface daily. NOAA/NESDIS provide the public with daily 25 km resolution of OSVW products.

The Advanced Scatterometer (ASCAT) is a new-generation European Space Agency (ESA) C-band scatterometer instruments at 5.2 GHz carried on MetOp launched in 2006. It has two sets of three antennae producing two 550 km-wide swaths. This instrument provide better resolution and over twice the coverage of its predecessors (the Active Microwave Instruments on ERS-1 and ERS-2) and achieve near global coverage in a period of five days. ASCAT provides 50 km resolution OSVW products.

Airborne scatterometers operate at significantly lower altitudes, on the order of 1 - 3 km. Thus they have finer spatial resolution, and are capable of studying detailed structure in severe weather systems. In the past, airborne scatterometers have been used for validation of satellite scatterometry results and for improvement of the forward models that satellite scatterometers depend on to derive global ocean surface winds [3]. The University of Massachusetts Amherst designed an airborne scatterometer, the Imaging Wind and Rain Airborne Profiler (IWRAP) [7]. This instrument is used to develop high resolution surface and atmospheric wind field products, expanding data sets scientists rely on for improving forecast models, and for increasing our overall understanding of severe storms at sea. IWRAP consists of C- and Ku-band Doppler radar systems capable of deriving ocean surface wind vectors based on scatterometry as well as atmospheric wind fields based on Doppler measurements [4]. It is an excellent tool for studying tropical storms due to its ability to map precipitation events. The high spatial resolution of IWRAP is able to determine wind variabilities of atmospheric events in regions where satellites are not capable of resolving.

1.2 Summary of Chapters

This thesis documents the operational state of IWRAP as of Fall 2007 and describes various system modifications made between 2005 and 2007. These modifications include improving the Ku-band subsystem's sensitivity and implementing an effective data processing method.

Chapter 2 provides an overview of IWRAP, its functions, a brief system description, and points out the system limitations. Chapter 3 addresses the work done on improving Ku-band system noise figure. It begins with methodology, then a detailed description of changes made to the Ku-band front-end. The impact of the change on radar system performance is addressed. Finally problems encountered during the improvement and solution to the problems are discussed.

Chapter 4 provide a brief overview of the data acquisition system as it was implemented in 2005. It mainly focuses on implementation of the pulse pair algorithm and the real time display. Chapter 5 discusses the field experiments conducted with IWRAP. A summary of the experiments conducted between 2005 and 2007 is given, and specifically, a winter 2006 experiment to develop high incident angle model functions is addressed. Finally, two particular storms in 2005 and 2007 are considered for sensitivity comparison before and after the front-end modifications. Chapter 6 provides a summary of work completed between 2005 and 2007, and offers suggestions for future work with IWRAP.

CHAPTER 2

IWRAP OVERVIEW

2.1 Scatterometer and Doppler Radar

A scatterometer is a calibrated radar that measures the backscattered power from distributed scatterers. Scatterometers are used to monitor vegetation growth, deforestation, soil moisture, sea ice activity, and near-surface ocean wind vectors [8]. IWRAP is a scatterometer that measures the ocean surface backscatters in order to derive wind vectors. The dominant backscattering mechanism from ocean surface for incidence angles from 20 to 70 degrees is attributed to Bragg scattering from centimeter-scale, wind-induced waves [6]. The amplitude of centimeter-scale waves, and their modulation by larger gravity waves, is highly dependent on the local wind conditions, which in turn have an effect on the backscatter response. An empirical relationship is used relating the backscatter to the wind condition, known as the Geophysical Model Function (GMF) [8] given by:

$$\sigma^0 = f\left(U_{10N}, \chi, \theta, \rho, \lambda\right) \tag{2.1}$$

where σ^0 is the normalized radar cross-section (NRCS), U_{10N} is the neutral stability wind at a reference altitude of 10 m, χ is the relative wind direction with respect to azimuth look angle, θ is the radar incidence angle, ρ is the polarization, and λ is the radar wavelength.

Figure 2.1 illustrates the relationship between backscatter response and the near surface ocean wind conditions. The wind direction dependence is illustrated by different backscatter response in upwind, downwind, and crosswind directions for one

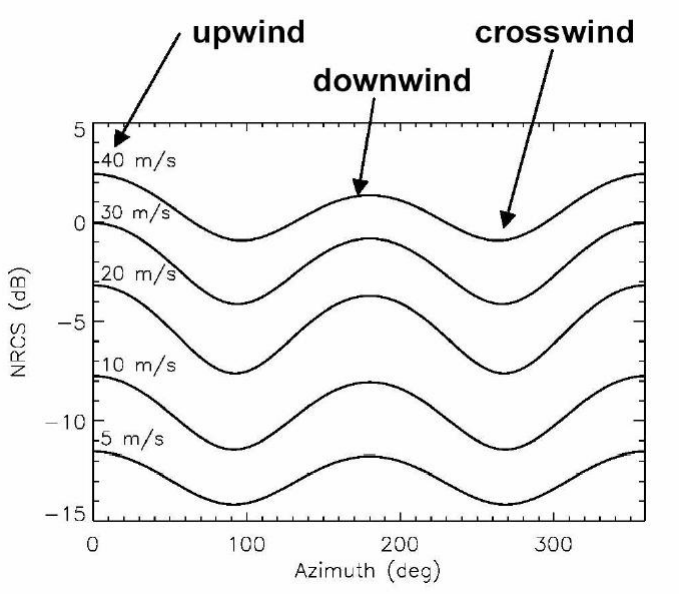

Figure 2.1. An example of the relationship between backscatter and azimuth direction for different wind speeds.

azimuth scan. Wind speed dependence is reflected in the mean NRCS value for varying wind speed. Due to the periodic nature of σ^0 in azimuth measurement, it is possible to represent it using a cosine Fourier series given by [9]:

$$\sigma^0 (U_{10N}) = A_0 + A_1 \cos\chi + A_2 \cos 2\chi \tag{2.2}$$

where A_0 is the mean σ_0 , A_1 represents the ratio of upwind to downwind σ_0, and A_2 represents the ratio of upwind to crosswind σ_0. The precision with which σ^0 is measured will greatly affect the Fourier coefficients and hence the estimation of GMF.

Besides being a scatterometer, IWRAP is also a wind profiler. As a range gated radar system where the entire duration of the transmitted pulse is sampled, IWRAP not only measures backscatter from the ocean surface, but also from atmospheric backscatter, namely precipitation. In tropical and extra tropical cyclones, more often than not, strong wind is associated with strong rain [7]. Thus, a Doppler radar is an

excellent tool for studying the inner structures of these storms, where the 3D wind field can be estimated within the sampled volume.

2.2 IWRAP Radar System Overview

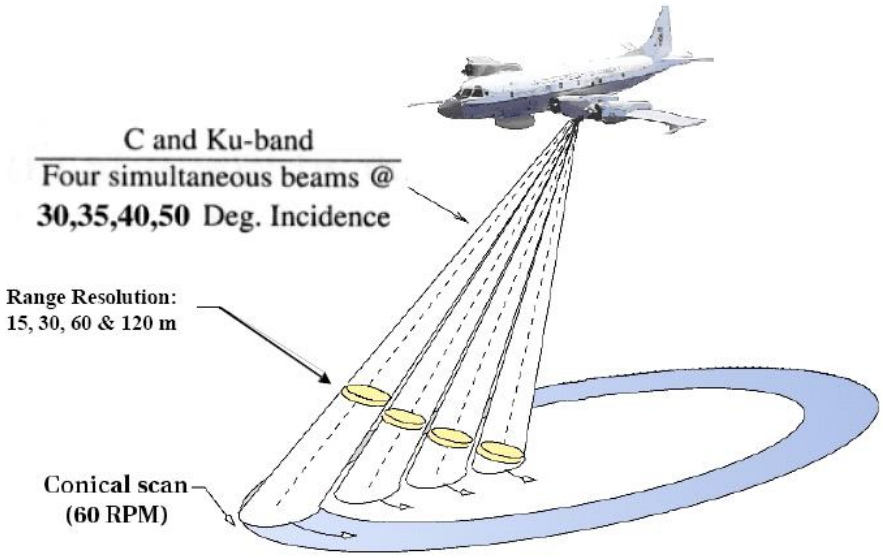

Figure 2.2. The measurement geometry for the IWRAP instrument.

IWRAP is a dual-frequency (C- and Ku-band), dual-polarization airborne Doppler radar system that utilizes multiple pencil beams at incidence angles from 20 to 50 degrees off nadir. Figure 2.2 illustrates the measurement techniques employed by this instrument. It scans the ocean surface conically at a rate from 30 to 120 RPM. IWRAP transmits 200 ns pulses which translates to a slant range resolution of 30 m. IWRAP transmits pulses at 20 kHz PRF to maintain a good balance between unambiguous range and Doppler velocity. Both PRF and pulse width are easily programmable to accommodate different flight and atmospheric conditions [7]. Figure 2.3 shows the IWRAP installation setup on the NOAA P3 aircraft. Table 2.1 lists the important parameters of the IWRAP instrument.

Parameters	C-band	Ku-band
IWRAP Radar systems		
Incidence angles (deg)	30, 50	30, 50
Tx Frequency (GHz)	5.42, 5.015	13.92, 12.87
Flight altitude (m)	1500 - 5000	1500 - 5000
Tx Power Peak (dBm)	48	49
Pulse width (ns)	200 - 800	200 - 800
Noise Figure (dB)	5	14
PRF (kHz)	1 - 100 (20 typical)	1 - 100 (20 typical)
Azimuth [deg]	0 - 360	0 - 360
Scan Rate (RPM)	15 - 120 (60 typical)	15 - 120 (60 typical)
Single-polarized antennas		
Gain (dBi)	26 - 29	25 - 28
E-plane HPBW (deg)	3.9 - 6.3	3.9 - 5.9
H-plane HPBW (deg)	3.8	3.8
Polarization	VV	VV
Dual-polarized antennas		
Gain (dBi)	22 - 26	22 - 26
E-plane HPBW (deg)	4.1-7.9(VV), 6.9-7.8(HH)	4.2-8.2(VV), 4.7-6.7(HH)
H-plane HPBW (deg)	6.5	6.5
Polarization	VV, HH, VH or HV	VV, HH, VH or HV

Table 2.1. C- and Ku-band IWRAP system parameter specifications

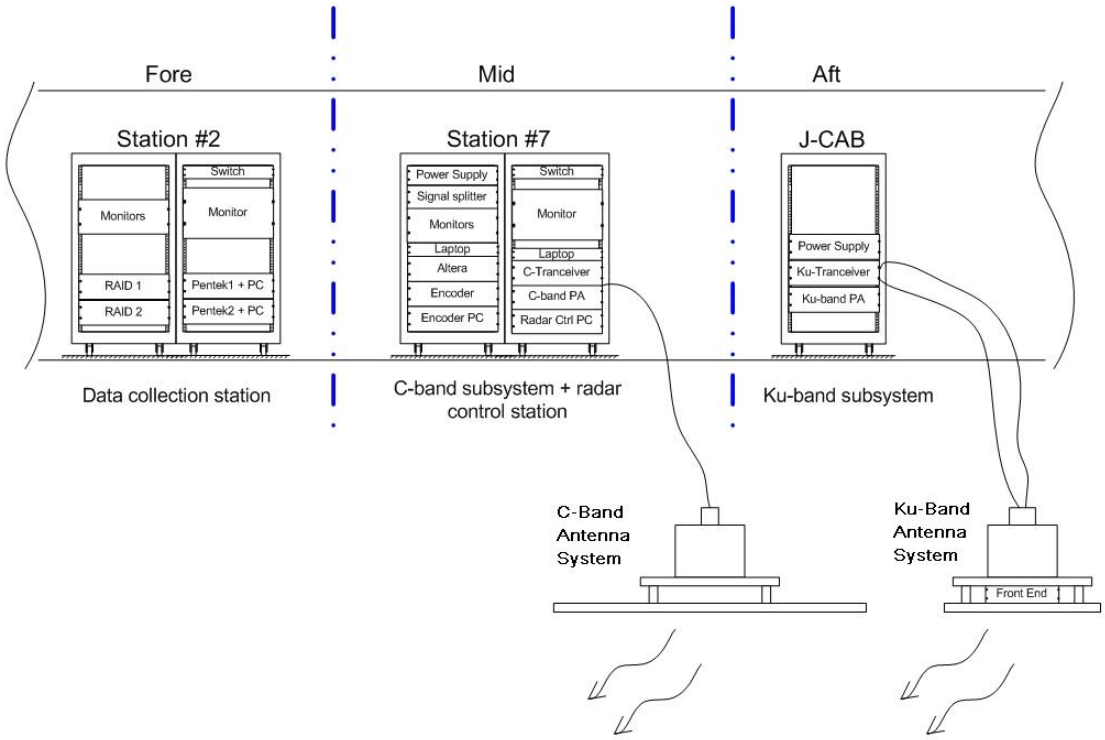

Figure 2.3. IWRAP installation aboard the NOAA P3 aircraft.

2.3 IWRAP Sub-systems Description

The C- and Ku-band transmitter/receiver systems are capable of operating independently. Both systems share a similar design, shown in Figure 2.4. Each system can be broken down into several subsystems: radar control, low-power transceiver, front-end, antenna, and the data acquisition subsystem.

The radar control subsystems generate all the necessary digital signals the radar systems require to operate. A Constellation 2K board from Nova Engineering company communicates via USB port with the radar control PC to generate timing signals for the IF and front- end switches for both C- and Ku-band. The PRF and the data acquisition system trigger are also generated from this board. This board is synchronized with the rest of the radar system using a 40 MHz reference signal generated in the radar IF (intermediate frequency) board. The IF board generate 10 MHz, 30

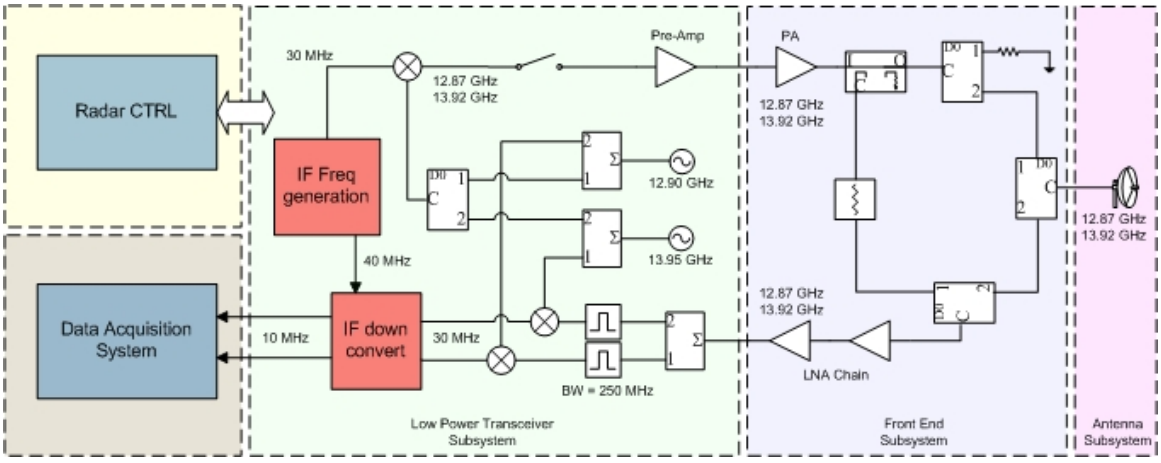

Figure 2.4. Ku-band system block schematic between 2005 and 2007 field campaigns, C-band system share a similar design

MHz, 40 MHz, and 80 MHz IF signals. These IF signals and the RF oscillators are synchronized to a 10 MHz STALO.

The antenna subsystems include the antenna which is a a frequency steered microstrip array, and the spinner assembly which allows the antenna to rotate at a constant rate. The rate of rotation is programmable between 15 - 120 RPM from Station 7 (the radar operation station). The encoder system that records the antenna azimuth position. The antenna generates pencil beams from 20 to 50 degrees for the specified frequency range of 12.8 GHz to 14 GHz for Ku-band and 5 GHz to 5.5 GHz for C-band.

The desired incidence angles are generated through RF oscillators located in the low power transceiver subsystems. In order to generate pencil beams at the desired incidence angles, two oven controlled RF oscillators at 5.045 GHz and 5.45 GHz for C-band and 13.95 GHz and 12.90 GHz for Ku-band were used as sources of RF signal to produce the desired incidence angles. During field campaigns between 2005 and 2007, 30 and 50 degree incidence angles were generated. There are also IF and RF

filters, as well as pre-amplifiers and IF amplifiers to bring received signals to the appropriate levels for the digital receiver.

The front-end subsystems contain all the high power RF switches to select between transmit and receive path, these switches are not only able to handle high power, they also have excellent switching times, rise and fall times, and RF signal isolation. The transmit/receive (TR) switch selects between the transmit path and the receive path at the antenna port. The cal/receive (CR) switch selects between calibration and the receive path, to allow the receiver to see either the attenuated transmit signal during the transmit cycle of the PRF, or to see the received signal from the antenna. The third and last switch is placed after the Microwave Power Amplifier (MPM), this switch is used to provide extra isolation to the receiver during the receive cycle. A low noise amplifier (LNA) is also in the front-end subsystems placed immediately after the CR switch.

The data acquisition subsystem accept 10 MHz IF signals, and performs final downconversion and digitization, initial processing of I and Q demodulation is done for Raw data mode. Data acquisition system and data packets formats are discussed in detail in Chapter 4.

2.4 Limitation of IWRAP in Precipitation

To understand the limitation to what scale of rain a radar can see at a certain range, it is important to see why that is and what parameters in the radar equation can be modified to improve it. We begin by looking at the meteorological radar equation

$$P_r = \frac{P_t G^2 G_s \lambda^2 c\tau\pi\theta_1^2\eta}{(4\pi)^3 R^2 l^2 l_r 16 ln(2)} \tag{2.3}$$

where

$$
\begin{aligned}
P_t &= \text{peak transmit power (kW)} \\
G &= \text{transmitting and receiving antenna gains} \\
G_s &= \text{system gain between receiving antenna and receiver} \\
\lambda &= \text{wavelength (m)} \\
c &= \text{speed of light, } 3\times10^8 \text{ (m/s)} \\
\tau &= \text{pulse width } (\mu sec) \\
\theta &= \text{transmitting or receiving antenna 3 dB beamwidth} \\
\eta &= \text{Radar volume reflectivity} \\
R &= \text{range to target (m)} \\
l_r &= \text{finite receiver bandwidth loss (dB)} \\
l &= \text{atmospheric loss (dB/km)}
\end{aligned}
$$

For meteorological targets, the backscatter of individual scatters σ_i is related to the radar volume reflectivity η by

$$\eta = \sum_i^N \sigma_i \tag{2.4}$$

Where σ_i is given by the Rayleigh approximation by

$$\sigma_i = \frac{\pi^5}{\lambda^4} D_i^6 |K|^2 \tag{2.5}$$

Where $K = \frac{n^2-1}{n^2+2}$, and where n is the complex refractive index for water. The Rayleigh approximation requires that σ_i is small compare to the wavelength, or $D_i \leq \lambda/16$ where D_i is diameter of the individual hydrometeor. With this approximation,

$$\eta = \sum_i^N \frac{\pi^5}{\lambda^4} D_i^6 |K|^2 \tag{2.6}$$

However in meteorological remote sensing, it is more preferable to use reflectivity factor Z, due to its independence of radar wavelength, λ. Reflectivity factor is dependent only on the diameter of the scatterer.

$$Z = \sum_{i}^{N} D_i^6 \tag{2.7}$$

Substituting Equation 2.7 in Equation 2.6 yields

$$\eta = \frac{\pi^5}{\lambda^4}|K|^2 Z \tag{2.8}$$

The received power P_r can be related to the reflectivity through the meteorological radar equation

$$P_r = \frac{\pi^3 P_t G^2 G_S \theta_1^2 c\tau |K|^2 Z}{2^{10}(\ln 2)\lambda^2 R^2 l^2 l_r} \tag{2.9}$$

Solving for Z to obtain minimum detectable Z or Z_{min}, when setting $P_r = P_n$

$$Z_{min} = \frac{2^{10}(\ln 2)\lambda^2 R^2 l^2 l_r P_n}{\pi^3 P_t G^2 G_S \theta_1^2 c\tau |K|^2} \tag{2.10}$$

Z_{min} is the minimum signal the radar system can detect. The C-band system is efficient in retrieving Doppler measurements under extreme rain conditions while the Ku-band is more efficient retrieving Doppler measurements from moderate to light rain [7]. This is because the Ku-band system is more sensitive to rain since the sensitivity is proportional to fourth power of the frequency. However, the attenuation of Ku-band signal through hydrometeors is significantly greater than its C-band counterpart [6]. Increasing sensitivity in Ku-band would expand the areas where retrieval of atmospheric boundary layer wind would be possible.

Past work [7] has shown that in the heavy rain condition exceeding 50 mm/hr, flying at a altitude of 3000 m, sampling rain down to the surface is only possible with the C-band system. Ku-band suffers severe attenuation by rain; signals are completely attenuated at a range of 1500 m at this rain rate and surface echo is below the noise floor. The Ku-Band system would be able to sample between range of 1000 m and 1500 m in light rain of 17 mm/hr and moderate rain of 31 mm/hr. Figure

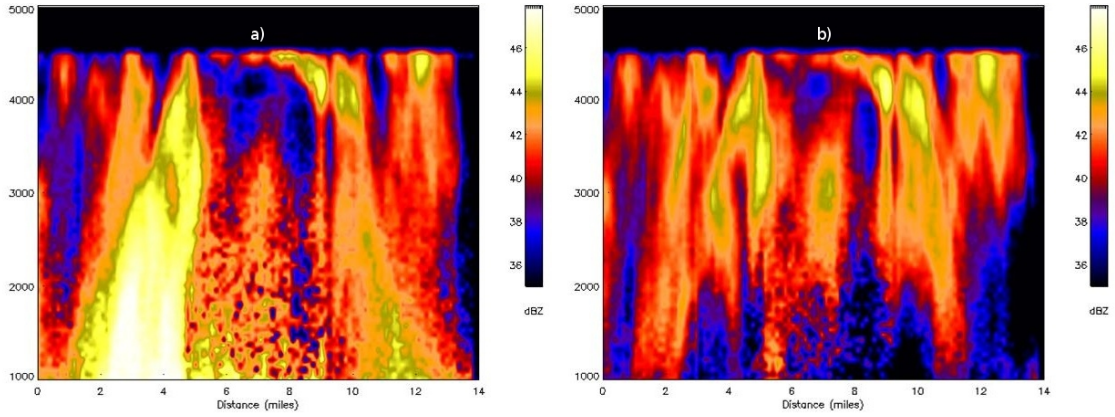

Figure 2.5. C-band (a) and Ku-band (b) reflectivity through an intense rain band during Hurricane Helene on Sept 18, 2006. Note the attenuation at Ku-band near the bottom of (b)

2.5 illustrates the attenuation effect, where Ku-band reflectivity is almost completely attenuated near the bottom of Figure 2.5b.

Ideally, it is desired to be able to observe the atmosphere all the way down to the surface and see finer rain distribution to help correct for attenuation. The advantage of sampling the entire volume at both C- and Ku-band is that the two wavelengths can be applied to help better quantify both reflectivity and atmospheric attenuation. With an improvement in sensitivity of roughly 7 to 10 dB, it will be possible to observe lower into the atmosphere with both C- and Ku-band frequencies under heavy rain conditions, which are common conditions during hurricanes.

Sigma-zero Error Variance:

Signal to noise ratio (SNR) plays an important role in retrieving radial Doppler velocity from precipitation as well as retrieving backscatter from the ocean surface. The NRCS is sensitive to changes in surface wind conditions. Within one full azimuthal scan, upwind and downwind measurements result in peaks while crosswinds result in nulls, as shown by Figure 2.1. A small difference in the peak measurements

will differentiate upwind from downwind, thus enabling derivation of the true wind direction. Large σ^0 error variance may hinder the ability to distinguish upwind from downwind, which would cause a 180^0 ambiguity in wind direction estimation. Another consideration is that through derivation of IWRAP GMF in past work [7], it has been shown that there is a saturation effect of σ^0 as wind speed increases, as shown in Figure 2.6, therefore, a low σ^0 error variance is even more critical at high wind conditions. Hence a key consideration in design would be to minimize the σ^0 error variance.

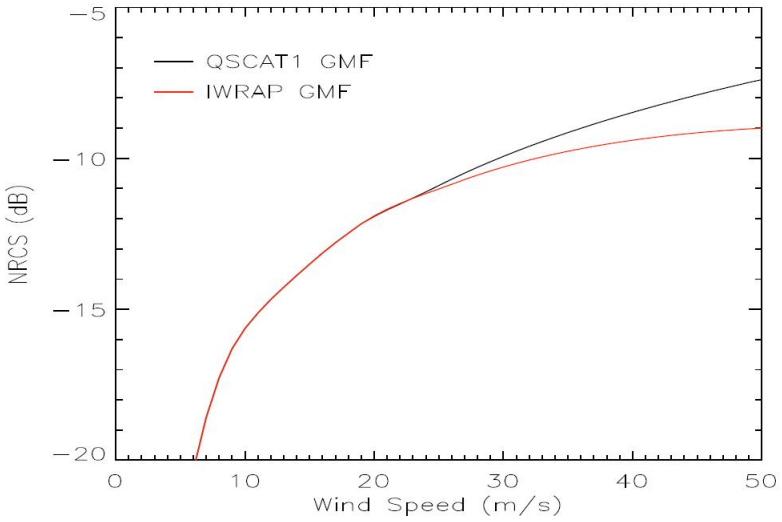

Figure 2.6. Upwind NRCS VV polarization at 54 degrees Ku-band.

To evaluate the precision of σ^0 it is common to use the K_p parameter [2], the normalized standard deviation of σ^0 is given by,

$$K_p = \frac{\sqrt{var\{\sigma^0_{meas}\}}}{\sigma^0} = \sqrt{\frac{1}{N_r}\left(1+\frac{1}{SNR}\right)^2 + \frac{1}{N_n}\left(\frac{1}{SNR}\right)^2}, \qquad (2.11)$$

where N_r is the number of averaged independent samples, N_n is number of independent samples of noise. NRCS precision is improved by increasing the number of independent samples or SNR. Figure 2.7 depicts this relationship.

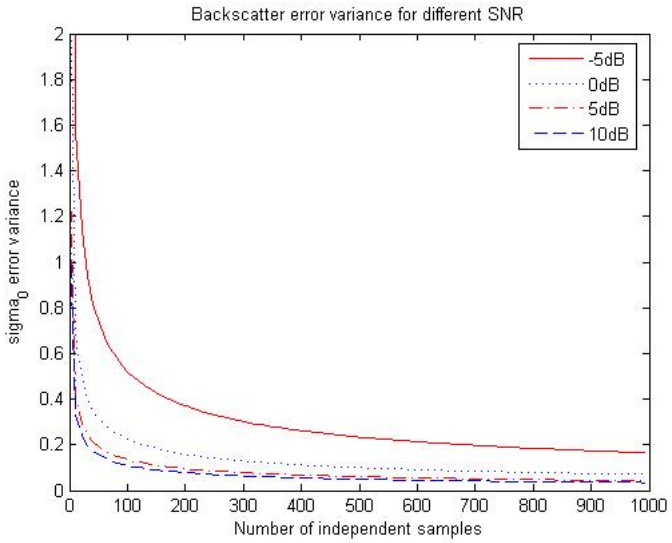

Figure 2.7. Backscatter error variance as a function of the number of independent samples for difference values of SNR.

N_r is dictated mostly by the rotation rate of the antenna [11]. It is often easier to achieve a better K_p by increasing the SNR. Consecutive profiles and several scans are averaged together to obtain a low σ^0 error variance, which however decreases spatial resolution. With higher SNR, less averaging is needed, thus providing better resolution for surface wind retrieval. However SNR improvement helps only when SNR is low. When SNR is moderate to high, only N_r will help the NRCS precision

CHAPTER 3

KU-BAND SENSITIVITY IMPROVEMENTS

3.1 Sensitivity Improvement Methodology

SNR is the single most important parameter considered for sensitivity improvement. There are two ways to increase SNR: 1) increasing the received power P_r by transmitting more power 2) decreasing the system noise power P_n. Due to the relative high cost of power amplifiers, increasing transmitter power was not an option. Instead, focus was put on decreasing the noise power. Consider the noise power equation,

$$P_n = kTBF \tag{3.1}$$

Where k is the Boltzman's constant ($1.38 \times 10^{-23} J/K$), T is the temperature in Kelvin, nominally ($290K$), B is the receiver bandwidth, F is the receiver noise figure, which is the measure of degradation of SNR between the input and the output of the receiver and it is given by $F_{system} = \frac{SNR_{in}}{SNR_{out}}$. Most receivers employ a number of gain stages, so the system noise figure depend upon the gains and noise figures of each stage according to Equation 3.2.

$$F_{System} = F_1 + \frac{F_2 - 1}{G_1} + \frac{F_3 - 1}{G_1 G_2} + \cdots + \frac{F_N - 1}{G_1 \ldots G_N} \tag{3.2}$$

In order to improve overall system noise figure, efforts should be made to improve the noise characteristics of the beginning stages, F_1, F_2, rather than later stages, F_{N-1}, F_N, because later stages have a diminishing impact on overall noise performance. The

low noise amplifier (LNA) is the first gain stage in the receiver chain, G_1. Best overall performance is achieved when the LNA has low noise figure and the loss between the antenna and the LNA is minimized.

3.2 New Design of Ku-band front-end Configuration

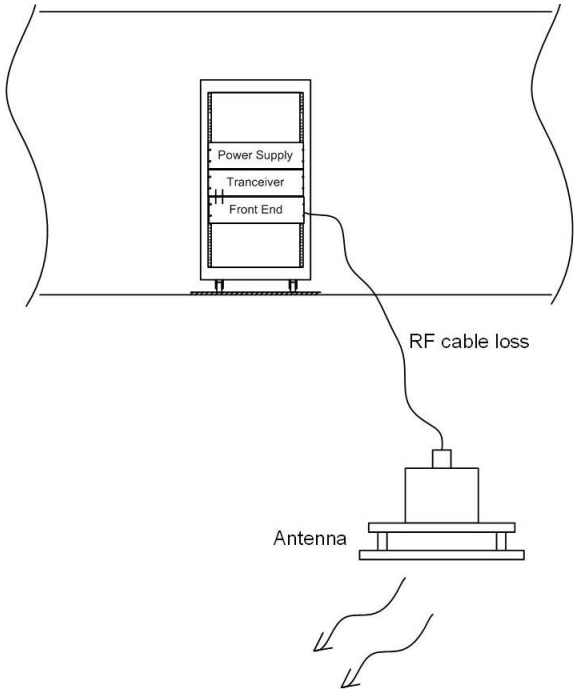

Figure 3.1. Setup on NOAA P3 to illustrate inefficiency in old Ku-band front-end

IWRAP's Ku-band front-end configuration was inefficient due to the physically large separation between the antenna and the front-end components. The radar antenna is part of the antenna assembly mounted on the belly of the NOAA P3 Aircraft illustrated in Figure 3.1. The radar front-end was located in a rack on the aircraft while the antenna is mounted on the belly of the plane. The front-end was connected to the antenna through a 2 m long cable with a one-way loss of 3 dB, and two cables of 0.5 m long of 1 dB each. This setup resulted in a fairly high overall system noise figure of more than 14 dB.

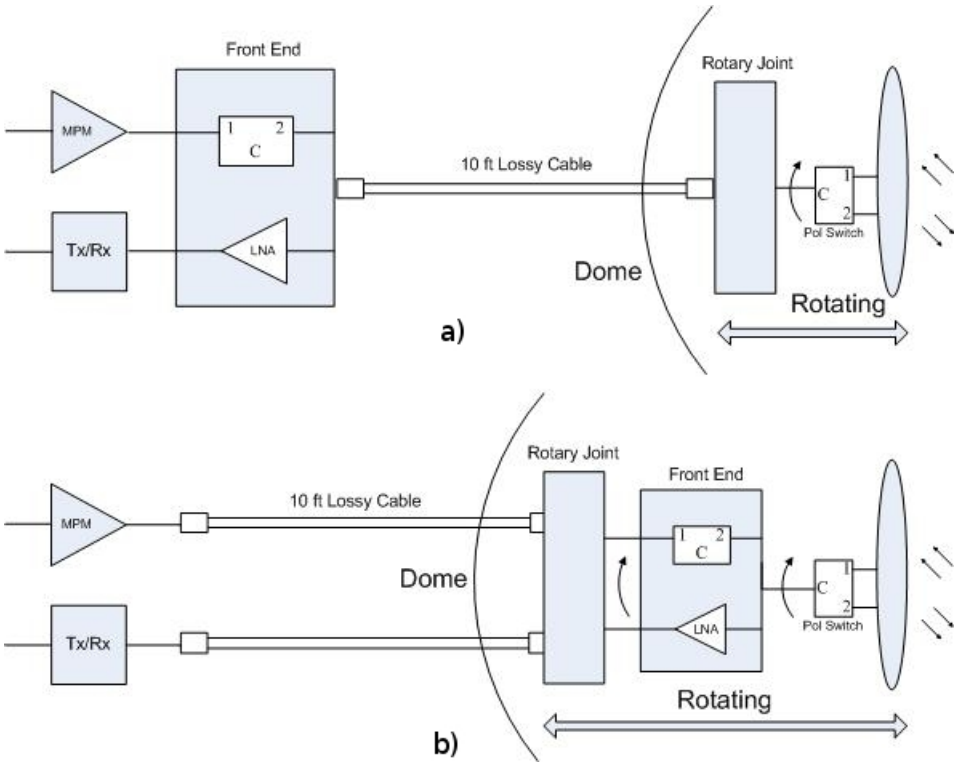

Figure 3.2. Ku-band system front-end modification block schematic. Old (a) and new (b) design

In order to reduce the noise figure, the front-end is modified by reconfiguring and relocating most of its components as close to the antenna as possible as shown in Figure 3.2. Relocating the front-end to the spinning portion of the antenna assembly was possible by a dual-channel RF rotary joint designed by Kelvin Engineering Company Figure 3.3a. A new 12 channel slip ring by Fabricast, Figure 3.3b, was also necessary to provide power and control signals to the rotating front-end components. Cable loss between front-end components and the antenna feed is reduced by moving total of more than 2 m of RF cables after the LNA, reducing overall first stage loss by more than 5 dB.

In addition to minimizing loss in the front-end, a new LNA with better noise figure was purchased from Miteq. The noise figure of the new LNA is 2.9 dB improvement over the old LNA. Comparison of the two LNA specifications is shown in Table 3.1.

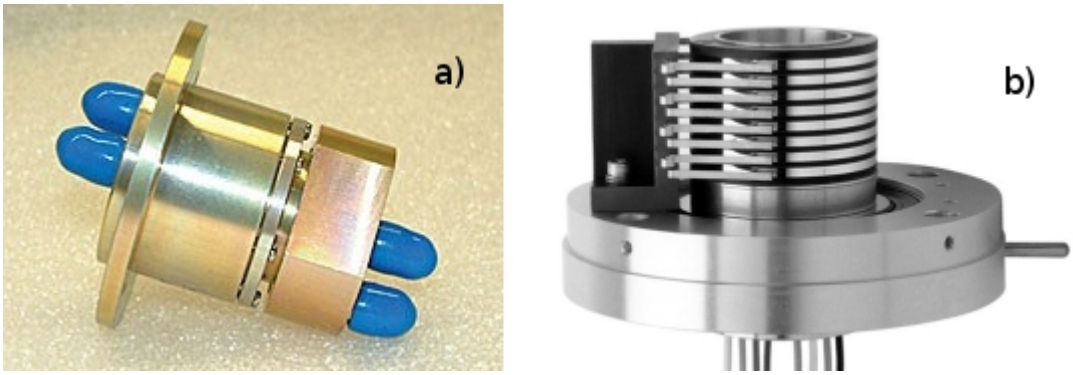

Figure 3.3. a) Kelvin Engineering Two Port SMA Rotary Joint, Min Isolation = 60 dB, b) Fabricast 12-ring slipring

Reduction in loss between front-end and the antenna feed, and the improvement of noise figure of LNA both contribute to the overall system sensitivity improvement. Table 3.2 summarizes the before and after total system noise figure. Overall system SNR improvement is predicted to be more than 7 dB. Old and new Ku-band front-end products are shown in Figures 3.4 and 3.5. The new front-end is installed on

Parameter	**Old**	**New**
Vendor	Miteq	Miteq
Frequency [GHz]	6 - 18	12 - 18
Gain [dB]	48.4	49.4
P_{out} 1dB [dBm]	22.25	13.5
Noise Figure [dB]	4.08	1.14
VSWR	<2.0:1	<2.0:1

Table 3.1. Summary of old and new Ku-band LNA parameters

Parameter	**Old**	**New**
Front-end losses [dB]	10	5
LNA noise figure [dB]	4.08	1.14
Overall system NF [dB]	14.08	6.14
NF improvement [dB]	-	7.94

Table 3.2. Summary of overall Ku-band system noise figure improvement

the antenna assembly shown in Figure 3.6 along with the rotary joint and slip ring. The antenna assembly is installed from the belly of the NOAA P3 aircraft, Figure 3.7 shows the setup with the radome removed.

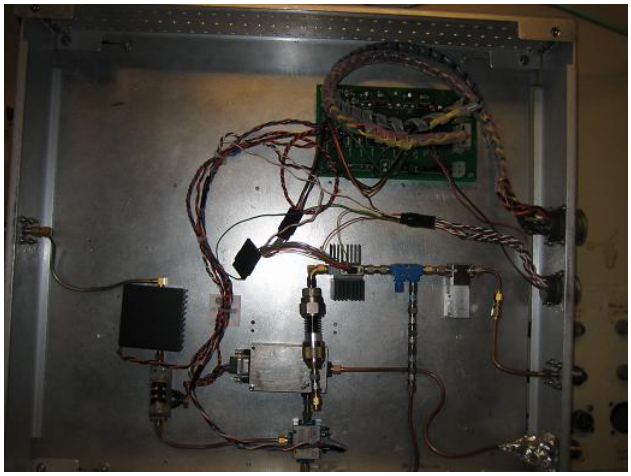

Figure 3.4. Old Ku-band front-end components layout mounted in JCAB rack.

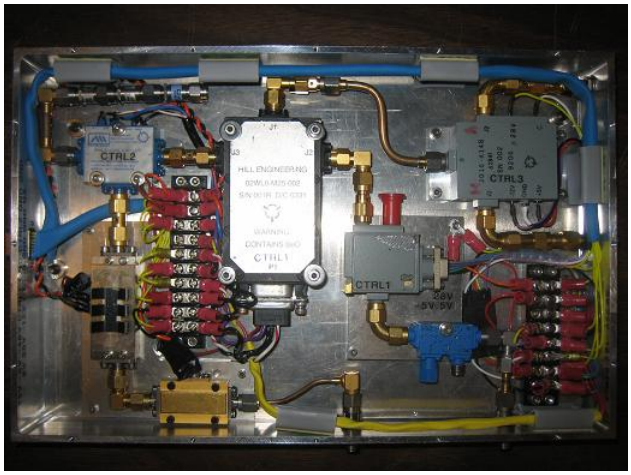

Figure 3.5. New Ku-band front-end after reconfiguration mounted on the spinning section of the antenna assembly.

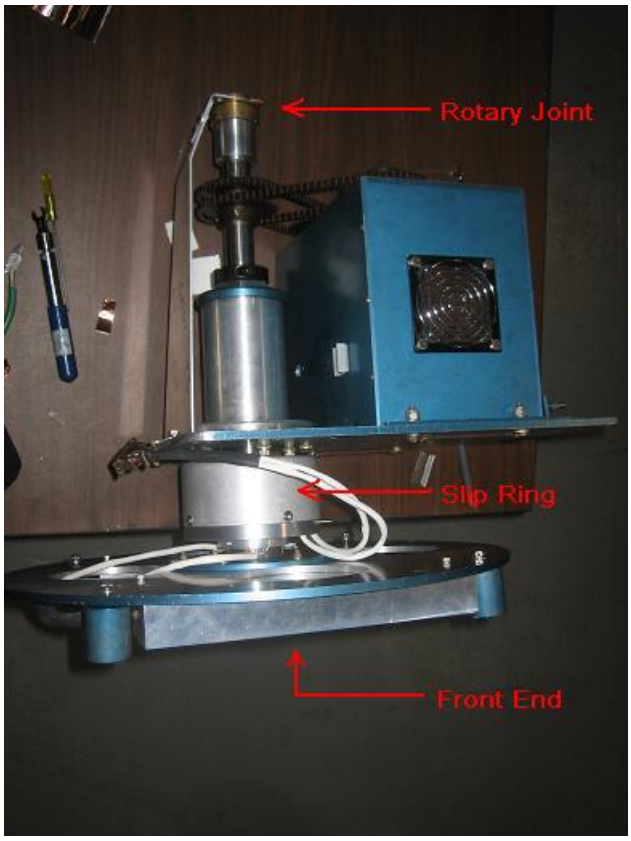

Figure 3.6. Spinner assembly with new slip ring, rotary joint, and front-end mounted on the antenna.

Figure 3.7. NOAA P3 Platform where the Ku-band antenna assembly is installed.

3.3 New Ku-band System Performance Analysis

With the sensitivity improvements, the Ku-band system is expected to observe more reliably the ocean surface while flying at a higher altitude, and to sample lighter rain which could not be detected before.

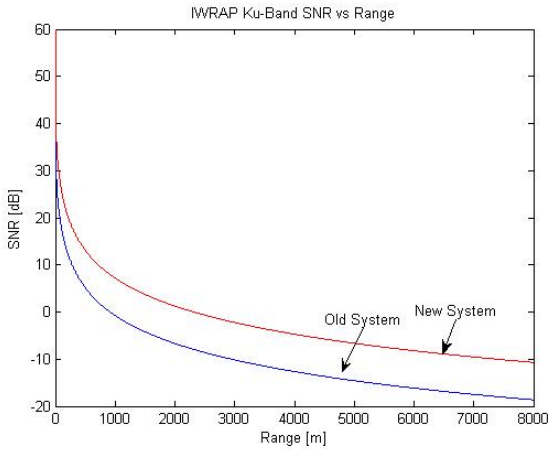

Figure 3.8. SNR versus Range for old and new Ku-band system, Rain rate = 5 mm/hr. Transmitted pulse = 200 ns.

It was previously stated that the Ku-Band signal in light rain was able to penetrate one km [7]. Figure 3.8 show why this is the case. Profiles with SNR below 2 dB are discarded. The SNR of the system prior to improvement falls below the threshold at roughly one km. The improved system would more than double the range, providing the capability to observe the entire volume under light rain. This also suggests that the improved system would achieve the same SNR as before but flying at a higher altitude. This would allow more flexibility when it comes to flight planning.

As shown by Figure 3.9, the old system was capable of seeing 35 dBZ at 3 km which translates to 5.37 mm/hr rain [9]. For the improved system 27 dBZ is observed, which translates to 1.44 mm/hr rain at the same range of 3 km. This suggests that the improved system will be able to see light rain, allowing an in-depth view of the atmosphere above the ocean surface.

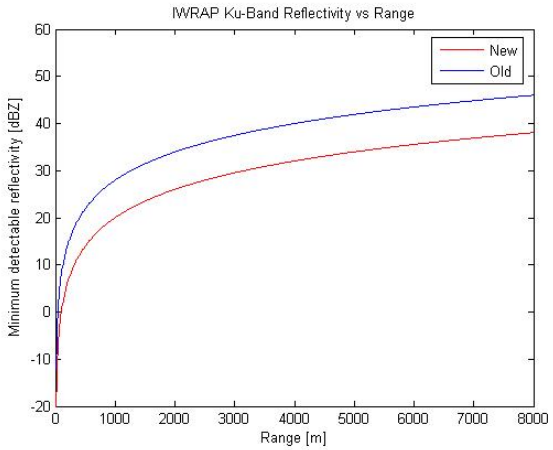

Figure 3.9. Reflectivity, Z versus Range for old and new Ku-band system.

3.4 Ku-band Calibration Loop

A calibration loop in a radar system is responsible for monitoring the transmitted power and any gain variations throughout the radar system. Therefore, the more of the system the calibration loop traverses, the more accurate the calibration signal is considered.

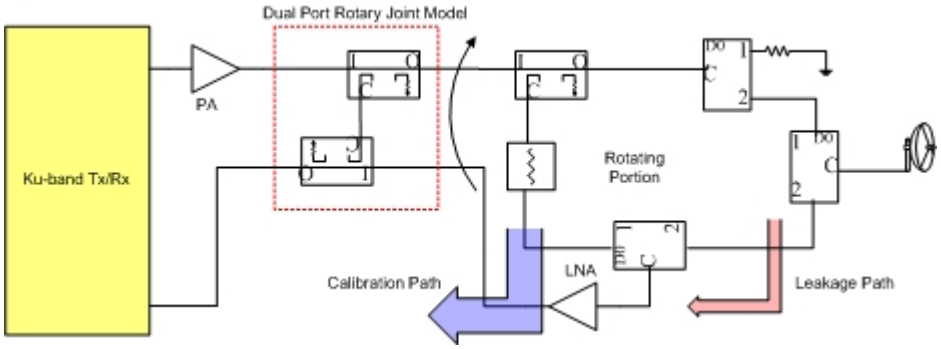

Figure 3.10. IWRAP Ku-band front-end showing calibration and leakage signal path.

The calibration signal is an attenuated version of the transmitted signal as shown in Figure 3.10. The attenuation is carefully chosen such that the calibration signal

progressing through the receiver gain stages remains within the linear region throughout. Any non-linearity may result in inaccuracy in tracking of the transmitted power.

While it is important to keep the calibration signal linear throughout the receiver, it is also important to maintain a low error in the calibration signal. The calibration sample is acquired during the transmit cycle of the Radar. Ideally, if the radar does not exhibit any leakage during transmission, the calibration signal can be any value as long as it remains linear within the receiver. In reality however, during transmission, some of the transmitted signal leaks into the receiver due to the finite isolation of the front-end switches. This leakage signal interferes with the calibration signal. In order to assure that the signal seen by the receiver is an accurate calibration signal and not corrupted by the leakage signal, the "calibration-to-leakage" signal ratio is usually kept to 40 dB. This ensures an error of no more than 0.1 dB by using Equation 3.3 and Figure 3.11. Isolation of the receiver is well characterized, the calibration signal is attenuated to a level 40 dB greater than the leakage signal. The calibration and leakage signal path is illustrated in Figure 3.10.

$$Calibration_{error} = 10^{\frac{P_{leakage}}{P_{calibration}}/20} \tag{3.3}$$

The new calibration path traverses more than 10 ft of cable loss, including cables in the front-end, the rotary joint, cables connecting the antenna which were not part of the old calibration loop. Thus IWRAP new internal calibration will be much more accurate compare to the old one.

3.5 Calibration Stability Problem and Solution

IWRAP's Ku-band sensitivity was improved by means of locating its front-end on the rotating side of the antenna assembly with a dual-channel rotary joint. However,

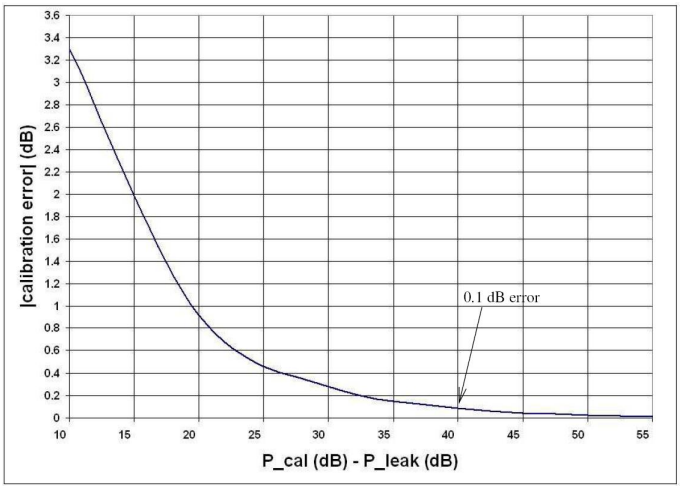

Figure 3.11. Calibration error versus calibration to leakage ratio

it was found that the stability of the calibration signal, or the calibration-to-leakage (CL) ratio was severely affected when the radar was installed on the plane.

When the front-end was in the original location on the NOAA P3 aircraft, the calculated CL ratio was 54 dB. However in reality, as observed by the data acquisition system, the CL ratio was only 38 to 42 dB when the antenna rotated while in normal transmit/receive mode. This resulted in +/-0.1 dB fluctuation in data, shown in Figure 3.12a, translating to an acceptable one percent error. When the test was repeated with the front-end on the rotating antenna, the CL ratio was reduced to only 8 to 24 dB. This resulted in a calibration pulse fluctuation of +/- 2 dB as observed in data, as shown in Figure 3.12.

The isolation of RF components was tested in both situations during operation and all were found to have the required isolation. The observed ratio in both cases differed significantly from expectation. However the problem is much more severe when the front-end is placed on the antenna. Data indicates that the CL ratio is dependent upon the azimuth rotation of the antenna assembly because it is highly correlated to the antenna azimuth position. This can be noted by the periodic nature

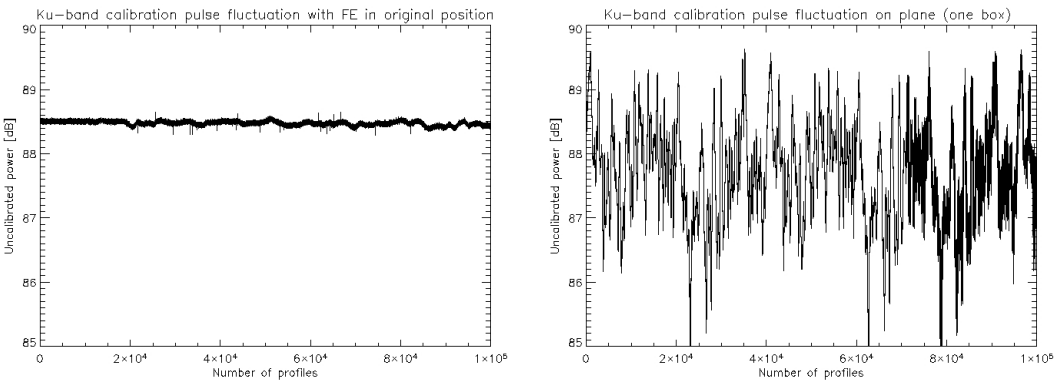

Figure 3.12. Calibration pulse fluctuation level before the front-end modification (a) and after the front-end modification (b) for a consecutive 10,000 pulses

of the calibration pulse fluctuation shown in Figure 3.12b. The fluctuation is either caused by the rotation of the rotary joint, the slip ring, or the antenna itself in response to the different surroundings azimuthally.

Diagnosis of Ku-band Calibration Pulse Stability Problem

The goal is to reproduce the problem back in laboratory from what was seen on the plane in the field by performing identical set of measurements. LNA was sent back to the manufacture to reduce the excess gain while maintaining the same 1 dB compression point such that there is more freedom to increase the calibration pulse strength. A set of S-parameter test were performed on all the front-end RF components. The S-parameter result indicated a problem in the isolation switch in the front-end with $S_{11} = 9$ dB. The switch was replaced with one of better S_{11} and isolation. Characteristics of the RF components were verified under high power operation, and results were in agreement with the S-parameter tests done with the HP Network Analyzer.

In the laboratory, where the test setup was identical to the installation in the field with the exception of plane environment and source of power, the CL ratio observed in data to be 14 to 29 dB when the radar operated in normal transmit/receive mode.

Calibration pulse fluctuation as observed from data to be +/- 1 dB. The CL ratio problem was still present but is not as severe as observed in the field.

When the calibration paths and leakage path in the front-end were disconnected and terminated with matched loads (in other words the transmitter and the receiver sections are completely isolated from each other with no direct RF path), upon turning on the transmitter, there still existed a signal 22 dB below the calibration signal. Likely culprits are the rotary joint, power lines that go from high power section (the transmit path) to the low power section (the receive path) in the front-end, and the close proximity of high power to low power subsections in front-end. This means although RF switches provide 54 dB isolation, the CL ratio would be no better than 22 dB. If one steps back in the receiver chain to further trace the source of the leakage, taking LNA and the front-end switch out of the picture but leaving in the dual channel rotary joint, one observes a signal 32 dB below the calibration signal, which indicates one source of problem is the rotary joint.

To summarize, the desired CL ratio is not achieved for two reasons: First, the rotary joint does not provide enough isolation such that leakage is observed only 32 dB below the cal signal when no other front-end components are connected in the receiver. Second, when LNA and the CR switch are connected, RF signal leaks into the LNA over the power lines and is amplified by the LNA yielding an undesired signal 22 dB below the calibration signal.

Solution to Ku-band Calibration Pulse Stability Problem

Rotary joint characteristics can not be altered easily, thus it is our fundamental limitation to the problem of the calibration pulse fluctuation. Rotary joint isolation was more than 60 dB as promised by the manufacture, however it is not enough isolation between the high power transmit path and the low power receive or calibration path. A possible solution is to amplify the calibration signal before the rotary joint

and then attenuate it by the same amount as the amplification after the rotary joint. This way the amplification is only applied to cal to actual leak and the attenuation would suppress all three signals: cal, leak, and rotary joint coupling. However this method is questionable due to the large amount of gain needed in the rotating section of the antenna assembly. To prevent even more problems, this method was set aside. Instead focus is set on how to mitigate the effect of power line coupling.

A solution for the power line coupling was successfully tested in the laboratory by supplying power directly from the power supply to each component in the front-end individually. Having all the front-end components in close proximity also introduced problems. Therefore it was decided to place high power components in one enclosure and low power components in a separate enclosure as shown in Figure 3.14. This way, the likelihood of the LNA picking up high power leakage signal was greatly reduced.

This setup allowed two sets of power lines separate from each other one for high power and one for low power electronics, minimizing power line coupling. Additional efforts were made to place appropriate capacitors and made sure ferrite beads existed on all front-end components to suppress fluctuating voltages. This proved to work leaving the CL fluctuation at the level which is limited by the rotary joint at +/- 0.5 dB, shown in Figure 3.13a. Final assembly of the front-end before the antenna is placed over it is shown in Figure 3.15

However, when the instrument was shipped and installed on the NOAA P3 aircraft, the fluctuation in cal pulse again increased to +/- 1 dB, shown in Figure 3.13b. The only difference was the plane environment, the difference in power supply and the location of the antenna. It is less likely for the environment or the power supply be a factor, and more likely due to the different environment surrounding the front-end. When instrument was back in the lab, the antenna assembly rested in a wooden box, on the plane, the antenna assembly is mounted and receded in a circular metal enclosure. When the antenna is lowered to be outside the enclosure, the fluctuation

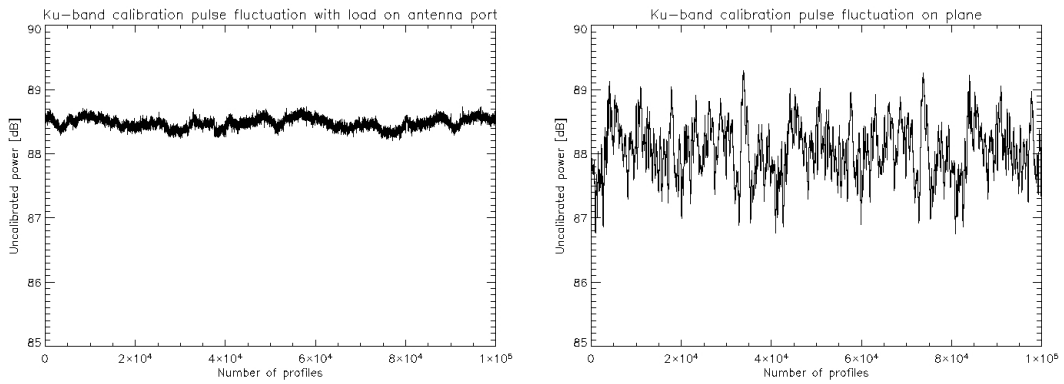

Figure 3.13. Calibration pulse fluctuation from only the dual channel rotary joint (a) fluctuation from installation back onto the NOAA P3 platform.

is same as measured back at UMass. Thus we conclude it is the reflection caused by the metal enclosure entering the receive path to affect the cal ratio. The solution at hand was to suppress the reflection as much as possible by lowering the antenna as much as possible without interfering with operation or safety protocols of the aircraft. Additionally we installed microwave absorbers rated at 40 dB on the inside wall of the metal enclosure, (Figure 3.16). Results from data showed that the fluctuation in calibration pulse is reduced by the installation of absorbers and the reconfiguration work. Figure 3.17 illustrates the level of fluctuations in the calibration pulse as observed by the data acquisition system for with the microwave absorbers. The calibration pulse fluctuation is contained to a level less than +/-0.5 dB.

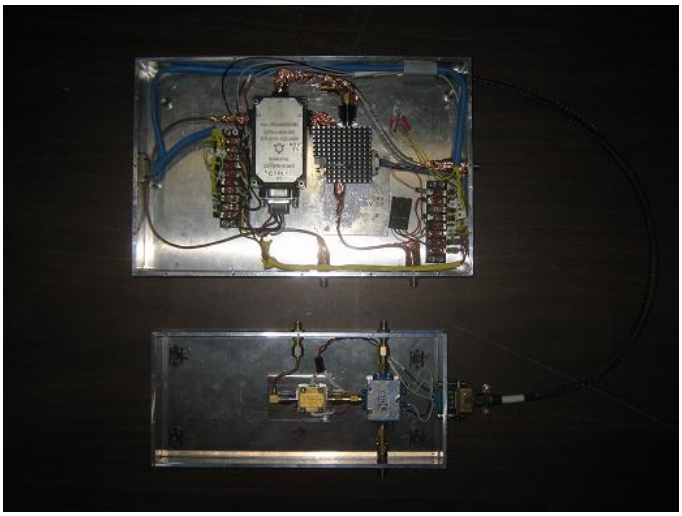

Figure 3.14. IWRAP Ku-band front-end was separated into high power and low power sections each in a separate enclosure.

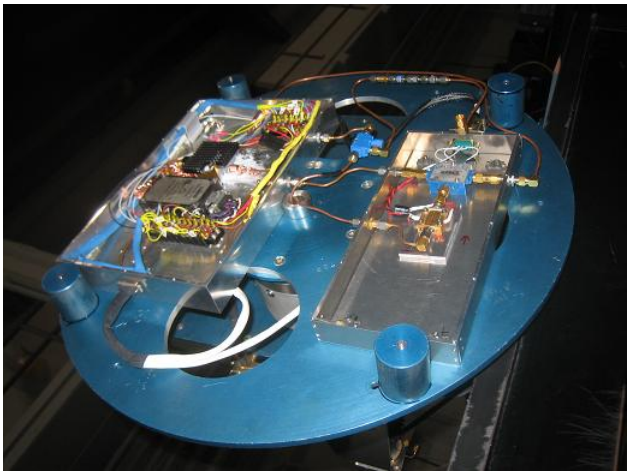

Figure 3.15. Two box setup mounted on the spinning portion of the antenna assembly.

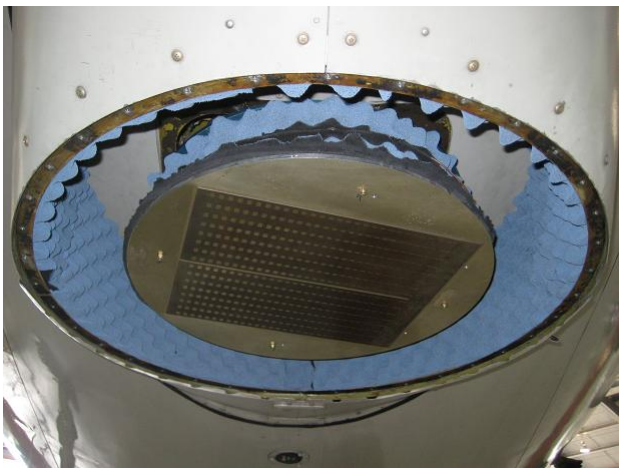

Figure 3.16. Ku-band front-end setup with 40 dB absorbers and antenna installed.

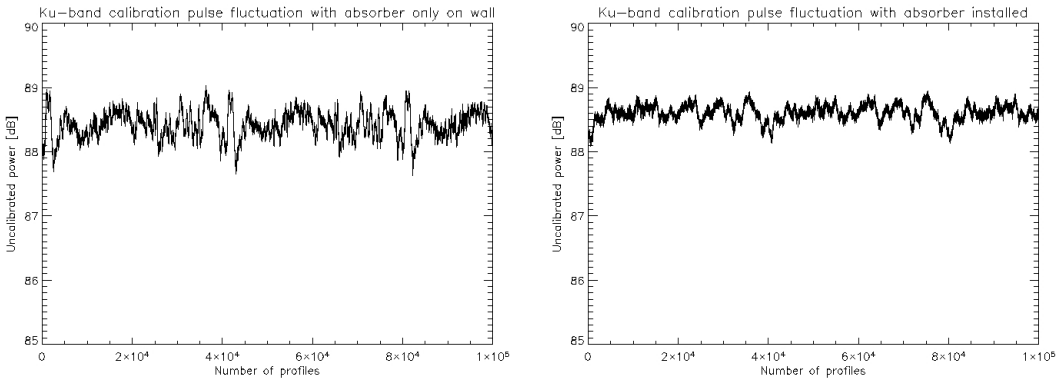

Figure 3.17. Calibration pulse fluctuation level with absorber along antenna enclosure wall (a) and with absorbers throughout (b)

CHAPTER 4

IWRAP DATA PROCESSING

4.1 IWRAP Data Acquisition System

A new data acquisition system was implemented in 2005 by Daniel Esteban Fernandez to serve two purposes: 1) to replace an aging FPGA-based digital receiver board, and 2) to enable capture of raw data for subsequent Doppler spectral processing. The data results presented in this thesis are obtained with this raw data system. It provides the ability to filter out or to remove surface backscatter contamination in the volume reflectivity measurements, and at the same time allow us to better quantify the impact of rain on ocean backscatter. However such a system has its disadvantages. IWRAP now has a more complex data acquisition system with more hardware and also orders of magnitude of more data to manage. In this Chapter techniques are introduced on how to deal with the immense amount of raw data and make it more manageable.

Figure 4.1 shows the computers with the rest of the IWRAP setup. There are now five computers involved in the operation of IWRAP. These include the original control computer (Beast), an encoder data acquisition computer, two radar data acquisition computers, and a real time display computer.

Prior to 2005 Beast was the only computer which handled radar control, data storage, real time display, and encoder data acquisition. Due to the immense data rate and the resource the raw data collection requires, these functions are now performed on separate computers. Beast now only functions as radar control, in which it communicates with the Altera Constellation FPGA board, provides programmable

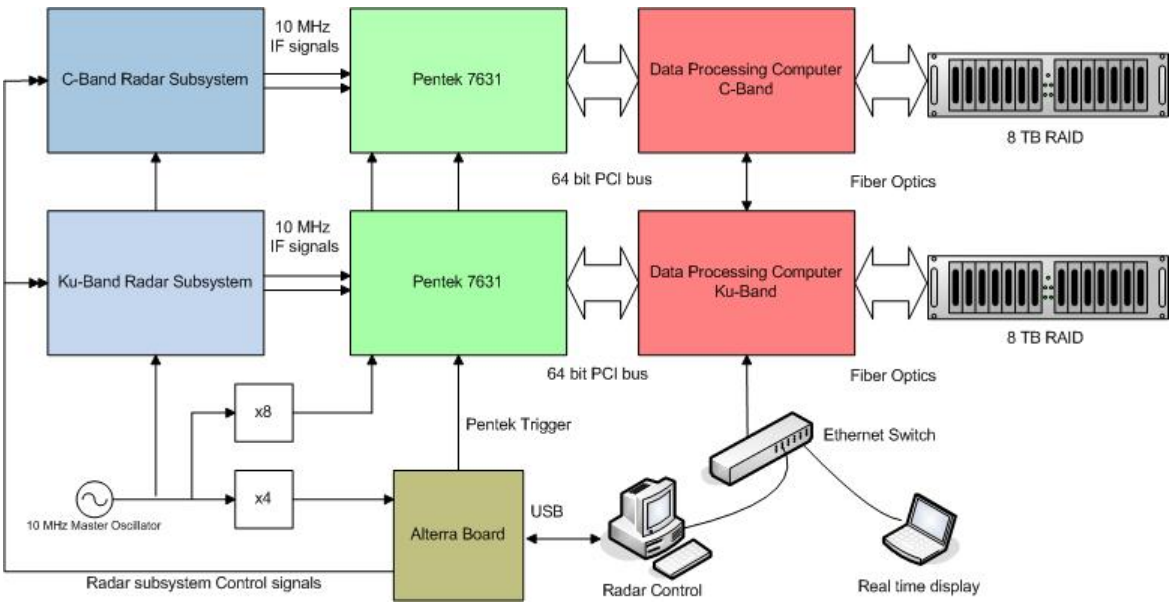

Figure 4.1. New IWRAP data subsystem block schematic.

pulse parameters to the board and enables and disables the radar timing, control, and PRF generation.

The four additional computers added by NOAA NESDIS each with a code name and a static IP:

- BigOther (192.168.0.231) communicates with the encoders and records the azimuthal position of the antennas, appending this data to the raw data files.
- Desire (192.168.0.226) and Fantasy (192.168.0.225) each house a Pentek 7631 digital receiver, performs final receiver downconversion and I and Q demodulation. Raw data are stored in RAIDS that are fiber linked to these computers.
- Unconcious (192.168.0.230) serves as a master control computer for data collection. Desire, Fantasy, and BigOther are enabled from this computer, it also handles the real time display which will be discussed in Section 4.4.

Digital Receiver

A Pentek 7631 digital receiver board is a replacement and upgrade to the aging GVA-290 data system for IWRAP described in [7]. The GVA was becoming less reliable, jeopardizing the ability to collect reliable data. The Pentek board has a 14 bit resolution A/D that samples the received IF signal at 80 MHz. It performs final downconversion from 10 MHz IF signals and is responsible for I and Q demodulation. Although the Pentek card is capable of having on board FPGA for doing more advanced real time processing, it is currently configured to only store I and Q, resulting in a immense data volume. The data rate is given by

$$DataRate = \frac{N \times N_o B \times PRF}{M} \tag{4.1}$$

Where N is number of samples per profile, N_oB is number of bytes per sample, M is the number of averages performed on raw data samples. IWRAP has four IF channels directed to two Pentek boards. For each channel on each board, there are 250 samples per profile. A 14 bit A/D results in 2 bytes each for the I and Q components. Nominal PRF is set to 20 KHz. The current system is set to pure raw data mode and does not perform any averaging. The system is configured to sample almost at 100 percent duty cycle, the effective data rate is approximately 20 MB per second per channel. A typical flight is usually 8 hours in duration. By the end of the day, IWRAP collects an estimated data volume of 2.3 Terabytes.

While raw data offers a new dimension in data processing, it is difficult to store and manage raw data at all times. Two 7 Terabytes RAID store the raw data. In order for the data to be useful and easily managed, an effective data processing algorithm must be developed.

4.2 Software Pulse Pair Algorithm

The Pulse pair algorithm is a method to estimate the first three moments of the Doppler spectrum [5]. The zeroth moment is the power, the first is the mean Doppler frequency shift, and the second moment is the bandwidth of the Doppler spectrum. This method is widely used in weather radar applications. The pulse pair algorithm reduces the data rate by orders of magnitude, by averaging many consecutive pulse pairs. This technique captures the phase difference between consecutive pulses and estimates the spectrum of the signal. Because frequency is very sensitive to phase errors, many consecutive pulse pairs are averaged to reduce the error in estimation.

This algorithm computes the magnitude and covariance estimate from two adjacent profiles and accumulates the result. The averaged magnitude can be expressed as:

$$\widehat{S}_{xx} = \frac{1}{M}\sum_{i=0}^{M-1} |V_{xx}|^2. \tag{4.2}$$

Where V_{xx} is the signal voltage and $_{xx}$ denotes the polarization of the signal. When the signal is demodulated into its I and Q components, an alternative expression is:

$$S_{xx}^{sum} = \frac{1}{M}\sum_{i=0}^{M-1} I^2 + Q^2. \tag{4.3}$$

The autocorrelation function at a time lag of Ts is be computed using

$$\widehat{R}_{xx}(T_s) = \frac{1}{M}\sum_{m=0}^{M-1} V_{xx_{i-1}} V_{xx_i}^*. \tag{4.4}$$

Likewise using I and Q, the alternative expression is:

$$R_{xx}^{sum}(T_s) = \frac{1}{M}\sum_{m=0}^{M-1} (I_{i-1}I_i + Q_{i-1}Q_i) + j(I_{i-1}Q_i - Q_{i-1}I_i). \tag{4.5}$$

From these expressions, the first three spectral moments are derived. The estimated signal power, which is equivalent to the autocorrelation function evaluated at zero time lag is obtained after subtracting the averaged noise power.

$$\widehat{S} = \widehat{R}_{xx}(0) = S_{xx}^{sum} - \widehat{P}_n. \tag{4.6}$$

The mean Doppler velocity is found by:

$$\widehat{v}_{Dopp} = \frac{\lambda}{4\pi T_s} \arg\left(\widehat{R}_{xx}(T_s)\right), \tag{4.7}$$

where λ is the wavelength The estimated standard deviation of the Doppler spectrum is:

$$\widehat{\sigma}_v = \frac{\lambda}{2\sqrt{2\pi}T_s}\sqrt{\left|1 - \frac{|\widehat{R}_{xx}(T_s)|}{|\widehat{R}_{xx}(0)|}\right|}sgn\left(1 - \frac{|\widehat{R}_{xx}(T_s)|}{|\widehat{R}_{xx}(0)|}\right). \tag{4.8}$$

The above pulse pair processing algorithm is implemented using the C programming language. As of now, this algorithm has been successfully tested during post processing. In the future it would be advantageous to implement this algorithm in real time such that it eliminates the need to collect raw data at all times, and allows a more rapid quick-look data assessment.

Position Pulse Pair Algorithm

While the pulse pair algorithm is capable of reducing data volume, there exist simultaneously a variant of the algorithm developed to utilize the azimuth antenna position when averaging instead of just averaging a preset value. This method minimizes the error from misinterpreting the azimuth position of the antenna when there is a variability in the rotation rate, this algorithm is illustrated in Figure 4.2.

Antenna position information is available with every acquired profile. The algorithm essentially creates a fixed number of bins per each antenna rotation. As profile position is read, each profile is placed in the appropriate bin. For the profiles in each bin, the power and covariance results are accumulated and the number of profiles per bin is remembered. Unlike the conventional pulse pair algorithm with a set number

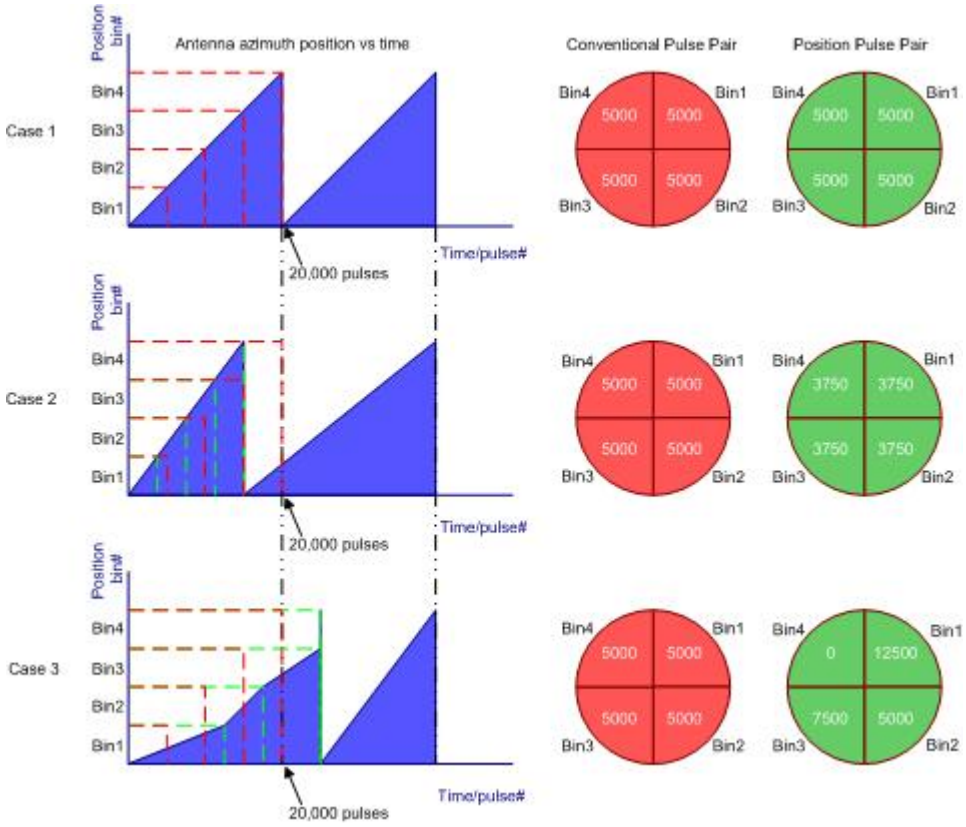

Figure 4.2. IWRAP Position Pulse Pair algorithm concept.

of profiles per bin, the number of profiles may or may not be the same for each bin. This algorithm eliminates the problem of antenna rotation variability by ensuring that a profile at a certain bin does not get accumulated and averaged with profiles of adjacent bins. The processing time of this algorithm as tested is competitive with the conventional pulse pair algorithm. A 1.5 GB file takes approximately 1 minute to process.

4.3 Real Time Display

Real time display for a radar system is needed in order to confirm its nominal operation. IWRAP needed a real time display program implemented for the raw data system on a computer other than the ones collecting the data in order to not

interfere with the raw data rate. Two forms of real time display programs were implemented; one shows signal power for every range gate and refreshes on a pulse to pulse basis, second one is in the form of a PPI plot displaying whole azimuth scan of reflectivity and Doppler velocity profiles and refreshes on a scan to scan basis.

Two data acquisition computers, Fantasy and Desire, process and stream raw data to RAIDs at a sustained rate of 20 MB/s. Any other concurrent processing job may interfere with this data rate. Thus, real time display program must be implemented on a different machine, Unconcious. Both data processing computers are configured to not only acquire raw data, but at the same time broadcast raw data over the network using the UDP protocol. UDP is used because it does not require handshaking with the client as does TCP. Any computer connected to the network is capable of acquiring data packets via the UDP data stream. A robust C-program was written to establish the network communication as well as writing the UPD data stream to a file, then an IDL program reads the written file and handles the processing and displaying of processed information on screen.

The first type of real time display is an A-scope display showing echo power vs range gate. It is used to monitor instantaneous radar signal return power level within the radar unambiguous range. This real time display indicates whether all channels of the radar are sotring valid data. It is capable of monitoring four channels by passing the appropriate parameters for port in the C program. As shown in Figure 4.3, it is possible to monitor the calibration pulse power, calibration pulse fluctuation level, existence of an ocean surface echo, incidence angle, distance to the ocean surface, and the signal to noise ratio. The C program takes a parameter of how many profiles to acquire at a time. The goal is to view profiles as quickly as possible, thus averaging is not desired and the number of profiles is set to 1. The IDL program takes the data and computes the power and display it on screen. The information proves useful, because all channels in the radar system can be viewed simultaneously such that any

problems would be evident in near real time. This display is used extensively at the beginning of every planned mission to check out the instrument.

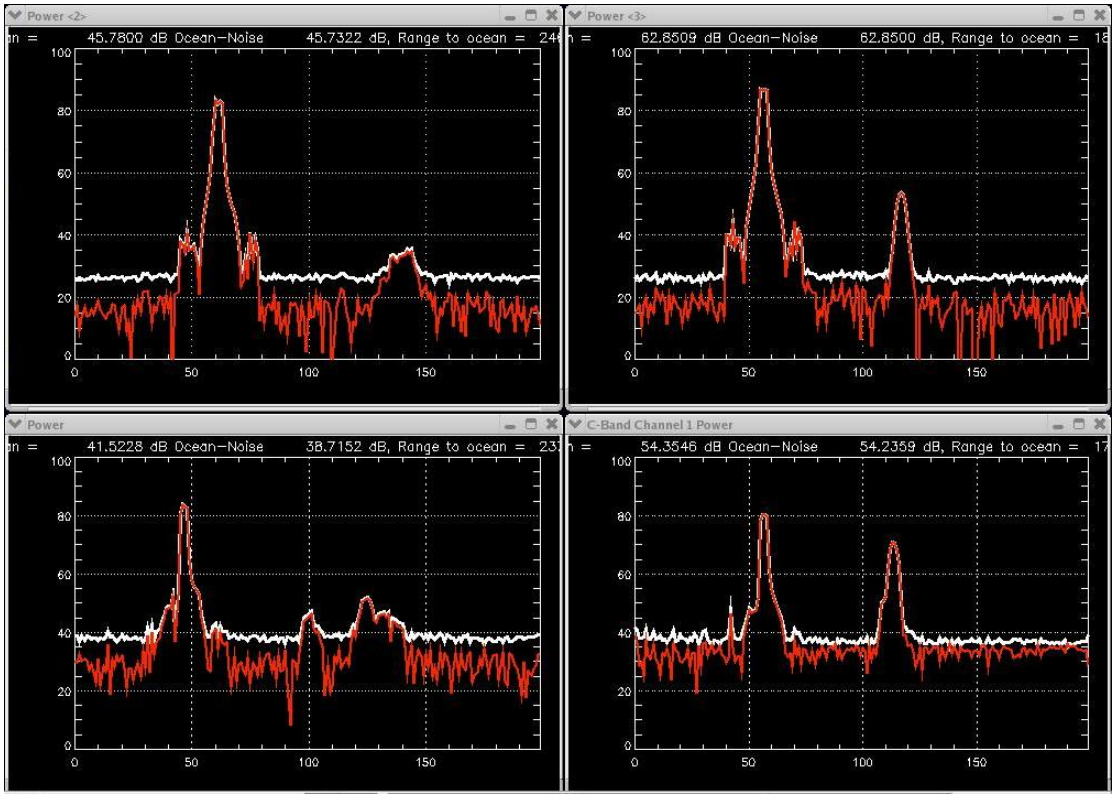

Figure 4.3. IWRAP power range gate real time display screen shot.

During actual data collection, it is desirable to have a more complete view of the data. IWRAP has an azimuth scanning antenna system, a common method of displaying real time information is through a PPI display, or plan position indicator. Essentially power and Doppler profiles are displayed in two separate polar plot on a per scan basis, where the center of the circular plot is the radar location and further from the center indicate further in slant range from the radar. This allows us to see detail structures in precipitation events and its effect on the surface backscatter. PPI is intuitive for individuals without a extensive radar background. The same C program used previously now may be programmed to dump the number of profiles that would fill one azimuth scan, in many cases that number is 20,000, then an IDL

program creates a 2D array of range gates and profile number. This display shows the ocean surface return, any precipitation is clearly visible between the center of the PPI plot and the ocean surface return on the outer ring. The refresh time for PPI is approximately 5 seconds due to computation time of the multiple profiles. The PPI real time display prove to be a more valuable and user friendly real time display and will be adopted for majority of the time during flights once everything works properly shown with the power range gate real time display.

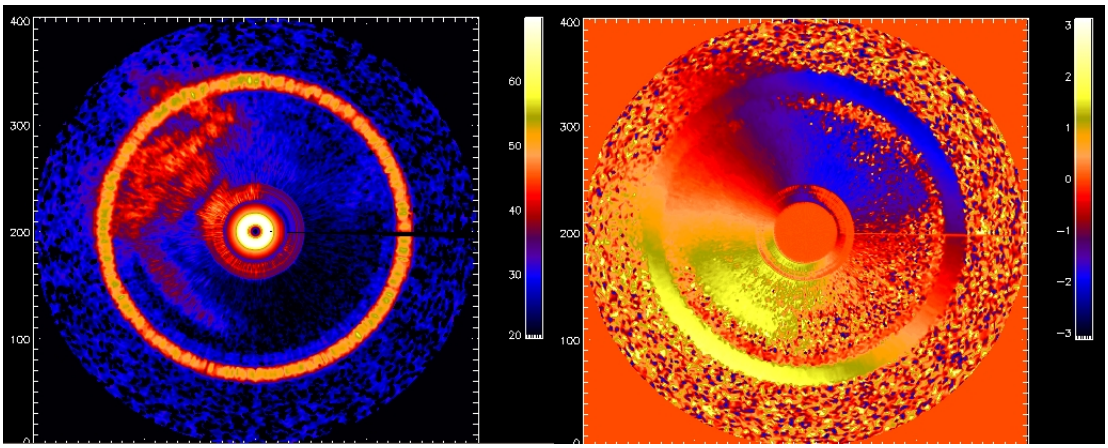

Figure 4.4. IWRAP polar real time display screen shot.

4.4 New Ku-band Encoder System

An encoder for a radar system is a device that tracks the antenna pointing position. For a radar with only azimuth rotation such as IWRAP, only azimuth position is acquired. IWRAP Ku-band had a 10 bit encoder which provided interpolated position value between bits, a higher number of bits encoder would provide real position data. For the reason to achieve better precision in our ability to resolve azimuth position for raw data processing, a 15 bit encoder was obtained and installed. Figure 4.5 compares the old and new encoder. It should be noted that only 12 out of available

15 bit are used for hurricane season 2007 due to the cable installation limitation on the NOAA P3 aircraft.

Figure 4.5. IWRAP 15 bit (New) and 10 bit (Old) BEI encoder system for the Ku-band antenna assembly.

A buffer board Figure 4.6 between the encoder and the PCI-7300A digital IO for storing encoder data is often used to protect the digital IO electronics. In case of excessive current, a replaceable buffer chip is destroyed as oppose to the digital IO. Collecting reliable encoder data was becoming an increasing challenge with the old encoder and buffer board combination, the old buffer board was the most likely culprit due to its complexity. A new buffer board with expanded inputs and simplified circuitry to the digital IO was re-designed, built, and tested by MIRSL student Joe McManus. Both the encoder and the new buffer board were implemented successfully. Figure 4.7 and 4.8 shows 12/15 bits of the new encoder in Grey code and decimal respectively. Buffer board schematics are located in the Appendix.

In order to verify the encoder bits are stored reliably when IWRAP antenna system is in operation, real time encoder display software was developed. One can monitor the azimuth scan angle in real time along with the azimuth display of raw data. The encoder bits are in Grey code binary format, an IDL program initially was used to plot all the bits to see if they are present, however this method was only allowed to

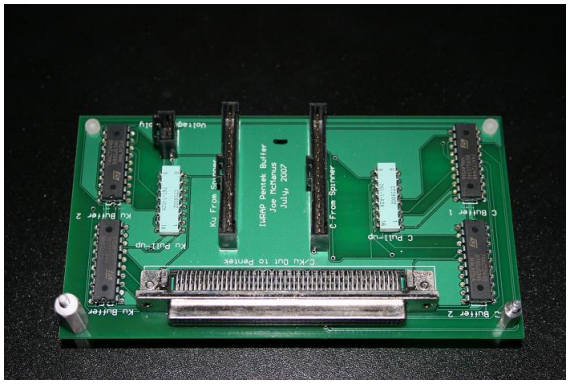

Figure 4.6. Ku-band encoder buffer board by MIRSL student Joe McManus.

look at an already collected file and only represented one instant of the operation. A real time program would prove more of value because it can catch a encoder problem instantly. A program was developed to align all the encoder bits, convert them into natural binary and then to decimal format, then the running sum of the encoder bits is plotted. The sum is reset once the antenna completes a 360 degree rotation. As a result, we're able to monitor the azimuth location of the antenna at the same time as the actual radar data is displayed.

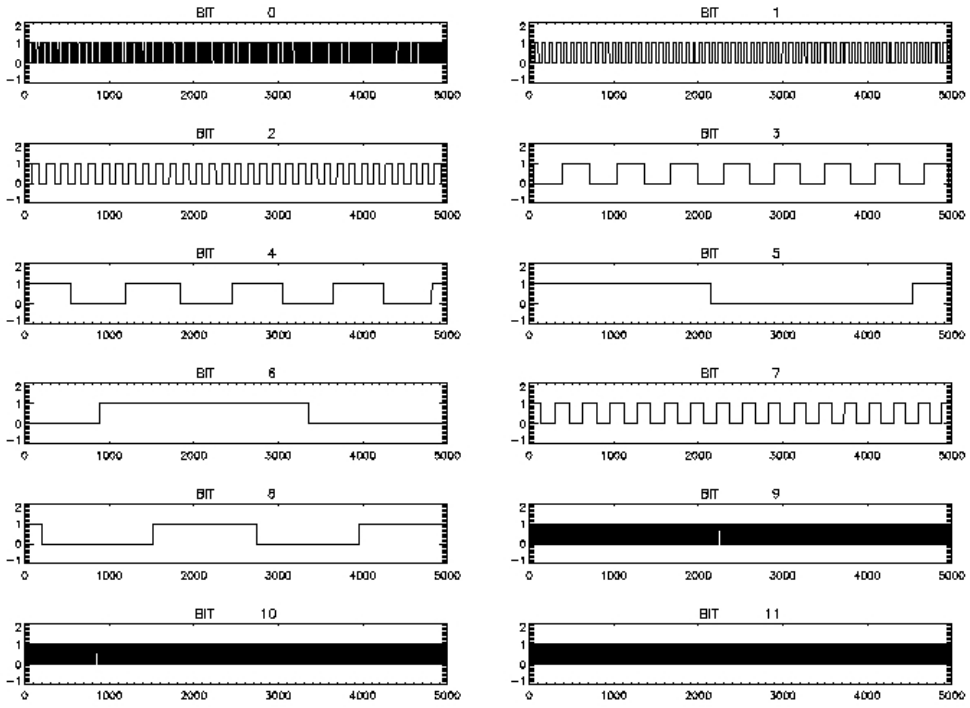

Figure 4.7. Grey code representation of top 12 bit of the new 15 bit Ku-band Encoder.

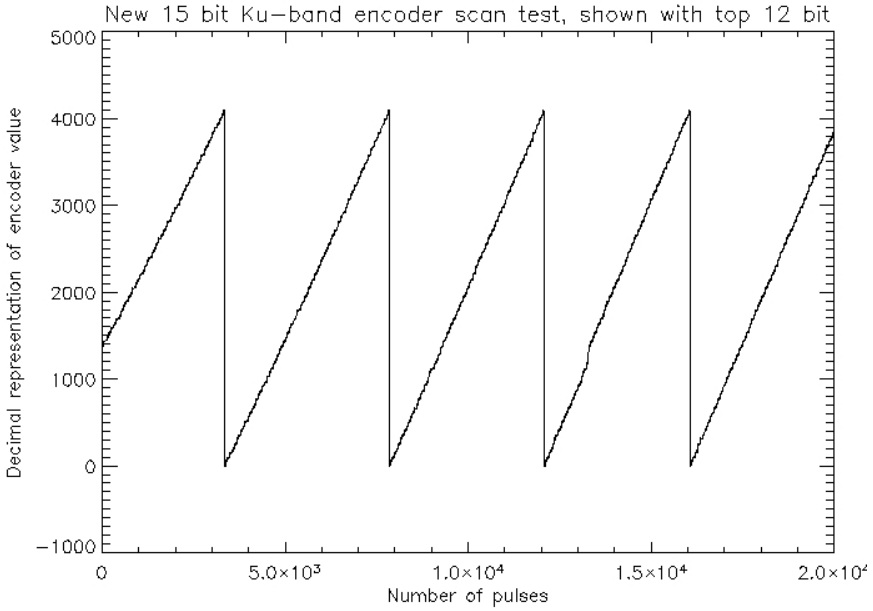

Figure 4.8. Decimal representation of top 12 bit of the new 15 bit Ku-band Encoder.

CHAPTER 5

FIELD EXPERIMENT RESULTS

5.1 Experiments Overview

IWRAP has been collecting valuable data since 2002, which contributed largely to the ocean vector wind community. IWRAP data were used in the development of the CMOD5 model function [1] , the model ASCAT depend on for ocean vector wind retrievals. It has developed high wind regime model function. IWRAP has continued to prove of value in satellite validation work at the same time expanding data sets used to study the effect of rain on backscatter measurements.

From 2005 to 2007, IWRAP was installed on NOAA P3 N42RF aircraft as part of the Ocean Winds project. Missions were flown in the tropics and extra tropics, during which a wide variety of atmospheric and oceanic conditions were sampled. Tropical storms experiments were conducted from Tampa, Florida and on occasion from eastern Caribbean islands, St. Croix and Barbados. The extra tropical storm missions departed from either St Johns, Newfoundland, Canada or Anchorage, Alaska. Many missions were planed in the vicinity of moored NOAA buoys and flight planning often involved coincident measurement with QuikSCAT and ASCAT satellites. Drop sondes, Bts, C-band belly radar, X-band tail radar, SFMR, are additional measurements provided by the P3 platform. The purpose of these experiments is to expand available data sets collected in different atmospheric conditions and to perform validation work for a recently ESA launched satellite, ASCAT. Raw data was collected for the first time, pulse pair techniques described in Chapter 4 were used to process the raw data. System improvements wwere made to Ku band to mitigate the attenuation problem

at Ku-band, allowing a more complete data set in C- and Ku-band. This chapter will give a summary of experiments conducted during 2005 to 2007 seasons. And then describe in detail one winter flight in 2006 when efforts were made to calibrate ASCAT. Results from data will be shown from before and after the Ku-band system modification. preliminary results are presented on spectral processing.

5.2 Experiments

Experiment Motivation

IWRAP can help address numerous questions in the ocean vector wind community. The British weather service among other agencies are interested to find out whether there exist different radar backscatter signatures of the same wind speed caused by different geographical location or temperature of the water. If so, this would introduce ambiguities in interpreting exiting model functions, there is only one wind speed associated with a certain backscatter power. This is the reason why IWRAP is involved in missions in the relatively warm tropics as well as the cold extra-tropics.

The effect of rain on ocean backscatter complicates the measurement process. The rain modifies the radar backscatter in three ways: 1) The radar signal is attenuated as it travels through the rain filled atmosphere resulting in under estimation, 2) the backscattered signal from rain contributes to the overall backscatter measurement resulting in over estimation, and 3) the ocean surface is modified by the rain such that the estimation of the backscatter becomes uncertain. Currently rain contaminated wind measurements from satellites are flagged, or simply not trusted for many applications. Unfortunately rain flagged regions are often also regions of strong wind, therefore areas of potential interest. This data could become useful data if the effect of rain is removed. IWRAP being a dual frequency instrument has the capability to observe the effect of rain at two wavelength. The C-band is less affected by rain and

can be used to correct the Ku-band measurement. Using two frequencies, the effects of the rain can be minimized.

The operational resolution of satellite data provided to the user community has 25 km resolution. Satellite measurements overlook many interesting features at smaller scales inside a tropical storm. IWRAP is capable of achieving 1 km resolution and can resolve the small features overlooked by satellite measurements. For global coverage satellite measurements are sufficient. IWRAP data proves more useful when it comes to resolving small scaled features.

Experiment Summary

From 2005 to 2007, IWRAP was involved in numerous field experiments, all of which were conducted on the NOAA P3 aircraft in combined research effort with NOAA NESDIS. Data were collected in tropical as well as extra tropical environments during variety of wind speed and rain rate events. Experiments were conducted at altitudes between 1500 to 5000 m. Table 5.1 summarizes the conditions which were sampled during that period.

Year	**Day**	**Storm Name (category)**
Sept 2005	6	TD16 (TD)
	7, 8, 11, 12	Ophelia (TS, 1, 1, TS)
	22, 23	Rita (5, 4)
Feb 2006	Several	Alaska (<20 m/s)
Sept 2006	16, 17, 18	Helene (3, 3, 3)
Jan 2007	20, 22, 26	St. Johns (<40 m/s)
Feb 2007	2, 6, 8, 9	QuikSCAT/ASCAT
Sept 2007	8/31, 1, 2	Felix (5, 5, 5)
	14, 15, 17	Ingrid (TS, TS, TS)

Table 5.1. Field measurement missions between 2005 and 2007, the category is based on the Saffir-Simpson Hurricane scale, category 1 - 5, TS = tropical storm, and TD = tropical depression

During hurricane season 2005, several major hurricanes made landfall in the United States (e.g. Hurricane Katrina and Rita). For the first time IWRAP collected raw data this season, providing spectral processing capabilities. The hurricane Rita data proved very useful because it had a range of wind speeds and rain rates, This was a category 5 hurricane with maximum wind of 285 km/hr

During winter season 2006, IWRAP deployed from Anchorage Alaska, flying near Kodiak islands. One mission entailed flying over Bristol Bay where sea ice would form every winter. More than three winter storms were sampled. None of the storms reached hurricane force wind conditions nevertheless, they included conditions of extra tropical storms.

In winter 2007, IWRAP deployed from St Johns, Canada. Most missions were conducted over the Labrador sea where winter storms are common before they reach western Europe. During the season efforts were made to validate ASCAT measurements, Hurricane force wind were observed in rain free condition.

Hurricane season 2007 included hurricane Felix, a category 5 hurricane that brought havoc to the western Caribbean and Yucatan peninsula communities. A total of three missions were flown through the storm. Many data sets of tropical storm force winds were collected. The various system modifications were tested for the first time this season.

5.3 High Incidence Angle Experiment

During February 2007 IWRAP participated in Metop's Advanced SCATterometer (ASCAT) calibration and validation effort by acquiring dual-band ocean backscatter measurements coincident with ASCAT's overpasses. Compared to the previous C-band satellite-based scatterometers such as ERS-1/2, for the first time ASCAT extends the range of incidence angles beyond 60 degrees. For these incidence angles the current model functions relating the ocean backscatter to wind vector are not

well known. In the presence of moderate to high winds, scattering mechanisms other than Bragg can become significant. For this airborne field campaign, IWRAP was modified to acquire ocean backscatter in the range of 50 to 65 degrees incidence to match ASCAT's highest incidence angle.

IWRAP is designed to scan the ocean surface between 20 to 55 degrees off nadir. Oscillators of different frequency are used to generate different incidence angles. A frequency synthesizer is used as an external oscillator to achieve the frequency required at the antenna to create a beam at 60 degrees incidence. A filter in the receiver selects the appropriate frequency and rejects all others during receive the cycle of the radar. There did not exist a filter for the synthesizer channel. To prevent interference from other channels, the synthesizer channel is transmitted last such that during receive, it would be the only incoming frequency.

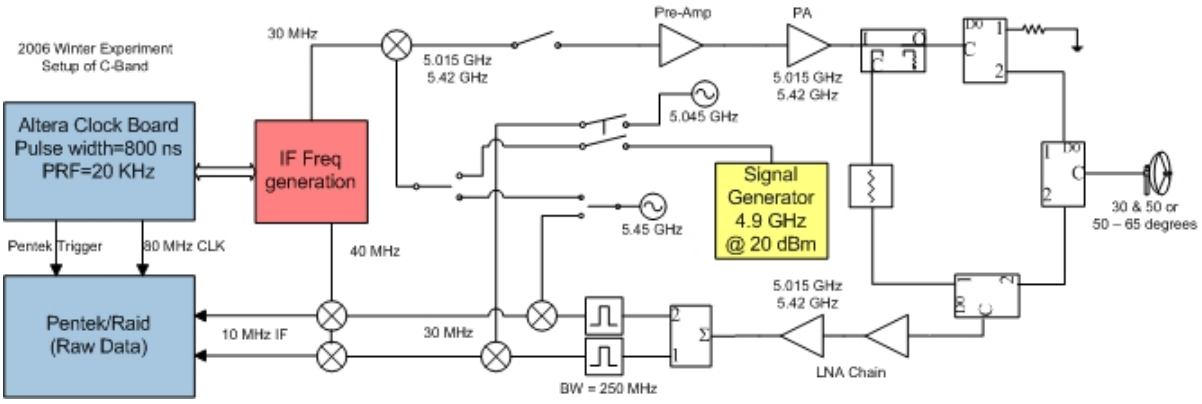

Figure 5.1. C-Band, Experiment setup during winter 2007 in St. Johns, Newfoundland, Canada.

The desired frequency is set as a CW signal out of the synthesizer integrated with the rest of the C-band system shown in Figure 5.1. Due to the fact that IWRAP was designed for 20 - 55 degrees incidence, all system components were designed to work with frequencies correspond to those incidence angles. Inputting frequencies to achieve 50 to 65 degrees was made possible but required fine tuning in frequency to

balance between maximizing power output and stay with the correct incident angle. At 4.9 GHz, there is only about a 3 dB drop in transmit power, the antenna beam is wider because input frequency lies outside of its specified range, SNR is sufficient for wind speed above 10 m/s, but insufficient for winds that are under. After achieving receiving ocean backscatter from 50 - 65 degrees, antenna pattern was not measured, instead it was derived from data by performing roll maneuvers with the aircraft up to +/-25 degrees.

During February, IWRAP flew a total of seven missions with the high incidence angle configuration. Wind speeds ranging from 5 to 50 m/s were sampled under virtually rain free conditions. One mission included sampling hurricane force wind which were in good agreement with QuikSCAT. In the past there has been hurricane force measured by QuikSCAT but were not validated due to the lack of ground truth.

For ASCAT validation, under high wind, IWRAP has enough SNR to cover a range of incidence angles between 50 to 75 degrees, preliminary work by Daniel Fernandez showed that at 16 m/s, IWRAP measurements agree well with CMOD5 and CMOD5.4 model functions up to 73 degrees incidence angle. However above wind speed of 16 m/s, IWRAP agrees better with CMOD5 than CMOD5.4 suggesting that CMOD5.4 should be tuned at high incidence angles for wind speed above 16 m/s. There is an ongoing effort to derive the full model function in the range of 50 to 75 degrees incidence angle for wind speeds from 15 to 50 m/s.

5.4 Hurricane Rita and Felix Pulse Pair Results

2007 hurricane season IWRAP operated with the improved Ku-band front-end. In order to demonstrate the improvement, a comparison of data before and after the system modification is performed. Pulse pair processing allows reduction of raw data size and carefully search through the data for potential regions of interest. Hurricane Rita and Felix data were chosen because they were similar storms both in strength

and in geographical location, making it more likely to find areas where comparison is relevant.

Experiments Description:

Hurricane Rita was among the top four most intense Atlantic hurricane ever recorded and the most intense tropical cyclone ever observed in the Gulf of Mexico. Rita was the seventeenth named storm, tenth hurricane, fifth major hurricane, and third Category 5 hurricane of the historic 2005 Atlantic hurricane season. Rita made landfall on September 24 between Sabine Pass, Texas and Johnsons Bayou, Louisiana, as a Category 3 hurricane on the Saffir-Simpson Hurricane Scale. The storm lasted from Sept 17 - 26, 2005. The maximum recorded wind speed was 180 mph, and lowest pressure was 895 mbar. Two missions were flown on Sept 22 and 23, 2005 into the storm when the maximum winds were recorded.

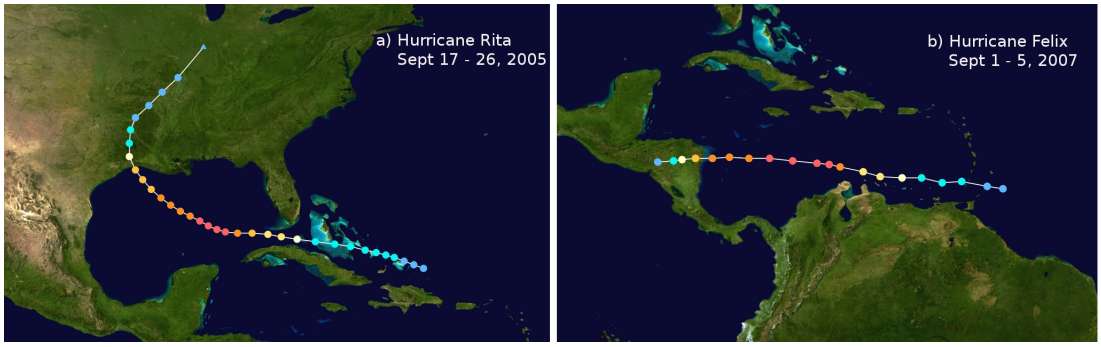

Figure 5.2. Hurricane a) Rita and b) Felix track.

Hurricane Felix was the sixth named storm, second hurricane, and second Category 5 hurricane of the 2007 Atlantic hurricane season. Developing from a tropical wave on August 31, it passed through the southern Windward Islands on September 1 before strengthening to attain hurricane status. A day later on September 2, Felix rapidly strengthened into a major hurricane, and early on September 3 it was upgraded to Category 5 status; by 2100 UTC, the hurricane was downgraded to Cat-

egory 4 status, but was later upgraded by 1040 UTC, September 4, to a Category 5 hurricane. Felix made landfall just south of the border between Nicaragua and Honduras in a region historically known as the Mosquito Coast. The duration of the storm was from Aug 31 - Sept 5, 2007. The maximum recorded wind speed was 165 mph, and lowest pressure was 929 mbar. Two missions were flown on Sept 1 and 2, 2007 into the storm during maximum wind.

Pulse Pair Processing:

Each raw data file for IWRAP is 1.5 GB, and it contains about one minute of data. It is impractical to work with raw data due to its sheer size. It may be more practical to process the raw data into smaller chunks using the pulse pair processor before the data is analyzed. The processing enables one to generate data products for an extended period of time without worrying about running out of storage space.

Using pulse pair algorithm discussed in Chapter 4, after averaging pulses together, it is possible to plot the averaged power for the accumulated profiles. Figure 5.3 shows the power plots of typical profiles showing two prominent features: 1) the power level of calibration pulse, the lower pulse being the ocean surface return, and 2) the noise floor. Many pulses may be averaged together to achieve a constant level of noise floor shown in Figure 5.3. Nadir return, and precipitation events are additional information and may be available on this plot.

Depending on the purpose of processing of the data, it may be more preferable to perform pulse pair algorithm to view the data by azimuth scan instead of a single profile. 20 KHz PRF and 60 RPM antenna rotation rate results in 20,000 profiles per scan. With this method, azimuth resolution is retained. when rain exist within the scan, clear rain structure is revealed within the illuminated volumn, Figure 5.4a. Doppler information is retained because azimuthal bins are separated, Figure 5.4b. For processing large amount of data, for reflectivity, whole scans of 20,000 profiles

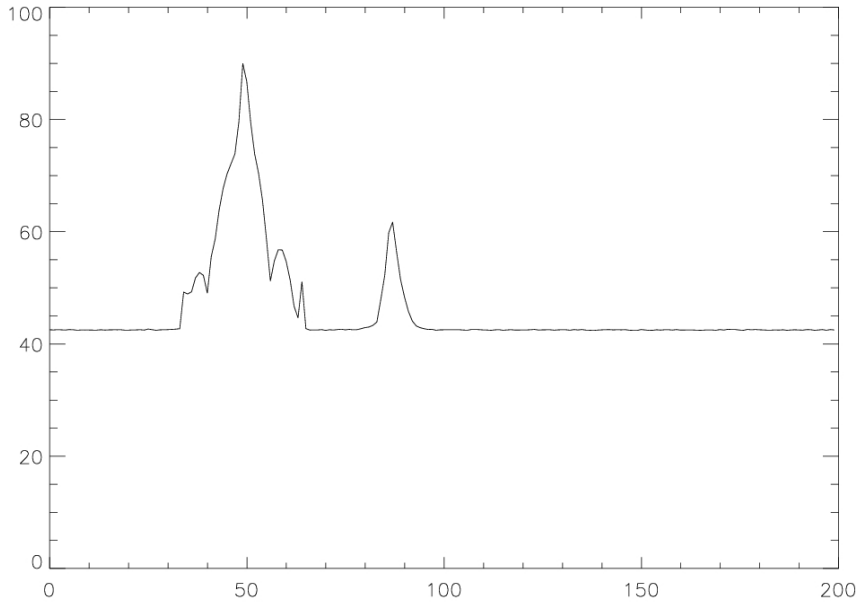

Figure 5.3. A typical pulse pair processed power profile, is shown un-calibrated power vs range gate, first peak is the calibration pulse, second peak is the ocean backscatter, anything in between higher than the noise floor is normally precipitation. Plot is shown in power vs range gate

may be averaged together. However for Doppler velocities, whole scans should not be averaged due to Doppler velocity's strong dependence on wind direction. It may be desired to average sections of the scan for multiple scans. The same can be done for reflectivity. Encoder information containing exact antenna azimuth position is of critical importance for this type of averaging.

Figure 5.5 is a power plot of altitude vs horizontal travel where whole azimuth scans are averaged together representing each vertical pixel, x-axis is showing a distance of 60 km, Doppler information is lost by this type of averaging.

Hurricane Rita and Felix Eye wall measurements

The eye wall of a hurricane usually houses the strongest winds and strongest rain of the storm, therefore it is the most extreme atmospheric condition one can

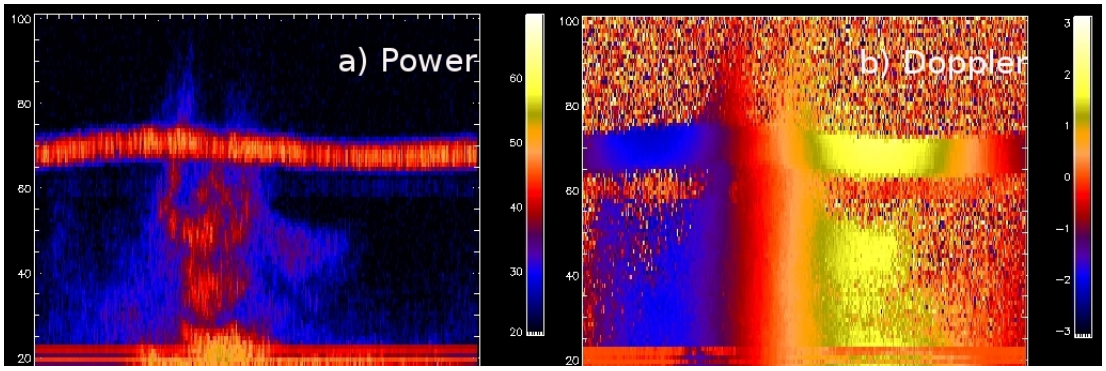

Figure 5.4. Pulse pair processing of a) power of 20,000 pulses or 1 azimuthal scan at 20 KHz PRF and 60 RPM antenna rotation rate. b) Doppler before aircraft velocity removal. Both plots are in range gates vs azimuth angle

encounter. Hurricane Rita and Felix both had wind in excess of 265 km/hr, and rain rates greater than 55 mm/hr in their eye walls. The attenuation effects on Ku-band would most likely appear the most detrimental in and around the eye wall of this storm. Thus it would be a good location for comparison of data before and after the Ku-band system modifications to see if sensitivity has improved.

The NOAA P3 has an array of in situ measurements of the temperature, pressure, rain rate, and also SFMR rain rate and wind speed. This in flight navigation data is appended to IWRAP data at the rate of 1 Hz. To narrow down search for eye wall data, times were recorded during the storm when eye wall penetration occurred. IWRAP raw data files contains time stamps, therefore it is easy to find the right data. Figure 5.6 shows a reflectivity equivalent plot of hurricane eye wall penetration on Sept 2, 2007 22:47 Z - 23:14 Z in hurricane Felix, shown along with SFMR Rain rate, wind speed, and radar altitude. The noise is subtracted, and the data is range corrected during processing. Figure 5.7 is the same as Figure 5.6 but for hurricane Rita on Sept 22, 2005 Z - 20:33 Z. Felix and Rita data sets were searched for a 40 mm/hr rain rate, resembling a moderate to heavy rain. A vertical slice, or an averaged profile is shown in Figure 5.8 for hurricane Felix and Figure 5.9 for hurricane Rita.

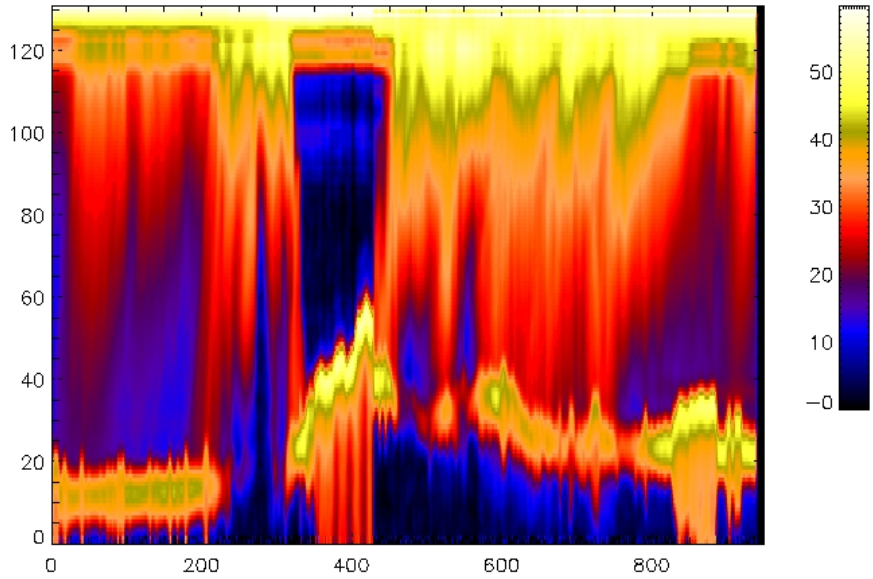

Figure 5.5. Power plot with respect to flying altitude (3km) vs horizontal travel (60 km)

Both profiles are shown with 20,000 averages, or one scan, with noise removal, and range correction. After taking account for the gain differences in the new calibration path in the modified Ku-band system, we can compare the dynamic range between the peak of the cal pulse and the noise floor from data profiles in Hurricane Rita and Felix. Figure 5.10 shows 20,000 averaged profile in both storms at 40 mm/hr rain rate. Even though the ocean echo in hurricane Felix profile is twice the distance away from the ocean echo in hurricane Rita, hurricane Felix profile maintains better SNR. This clearly shows that there is an improvement in sensitivity of the Ku-band radar.

Using pulse pair processing techniques, we deduced that the dynamic range on the lower end of the improved Ku-band system is increased. Therefore it is possible to sample lighter rain, and profile further down in the atmosphere.

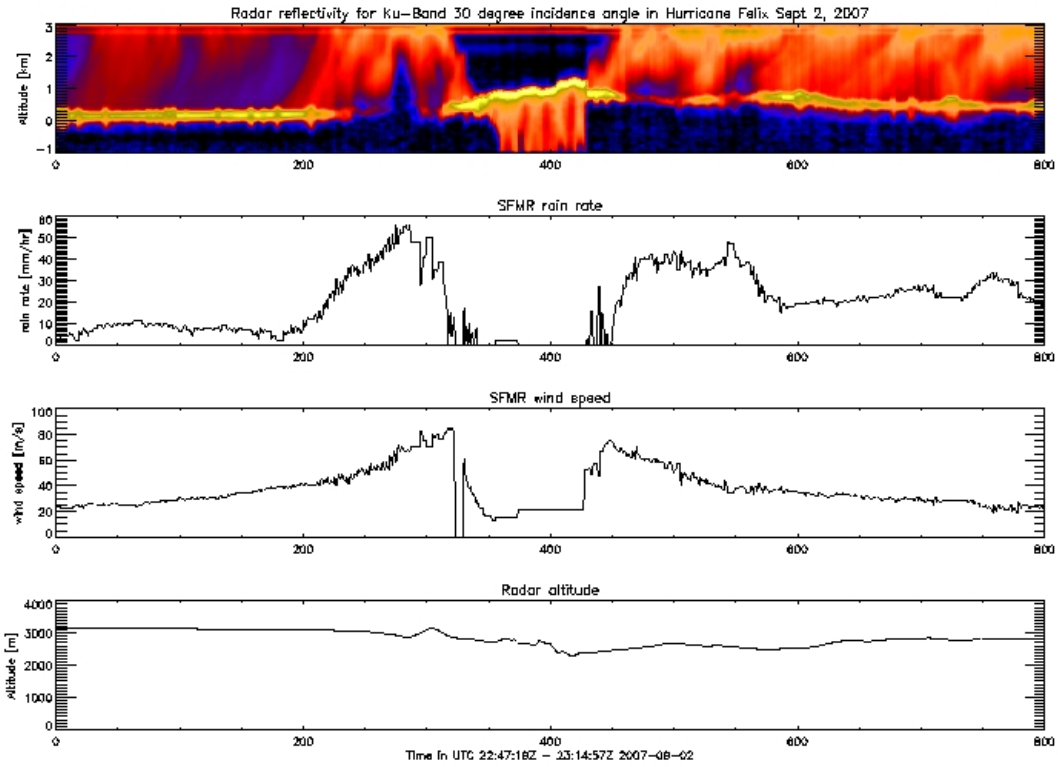

Figure 5.6. Hurricane Felix eye wall penetration with SFMR rain rate, wind speed, and flying altitude.

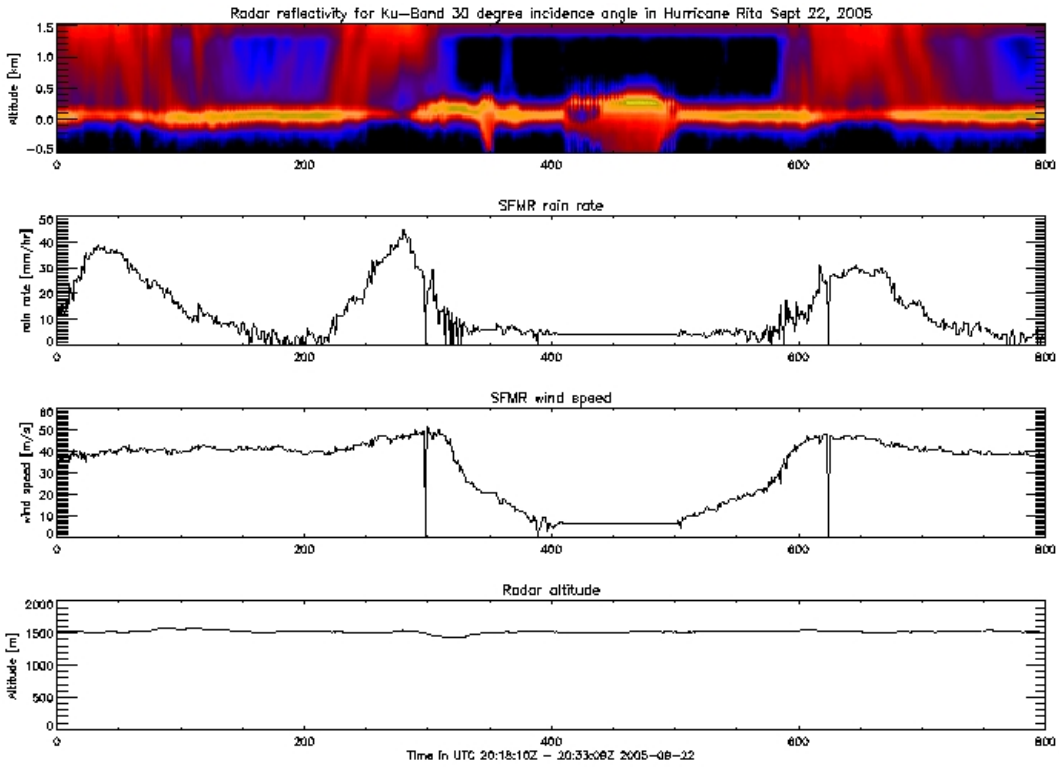

Figure 5.7. Hurricane Rita eye wall penetration with SFMR rain rate, wind speed, and flying altitude.

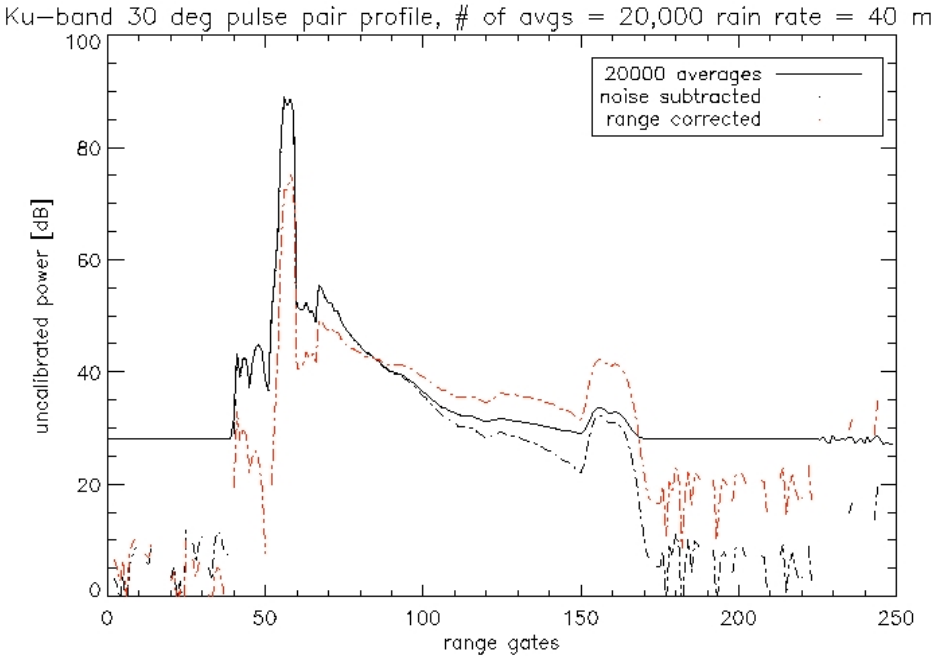

Figure 5.8. Hurricane Felix single profile at 40 mm rain rate shown with 20,000 averages, noise removal, and range correction.

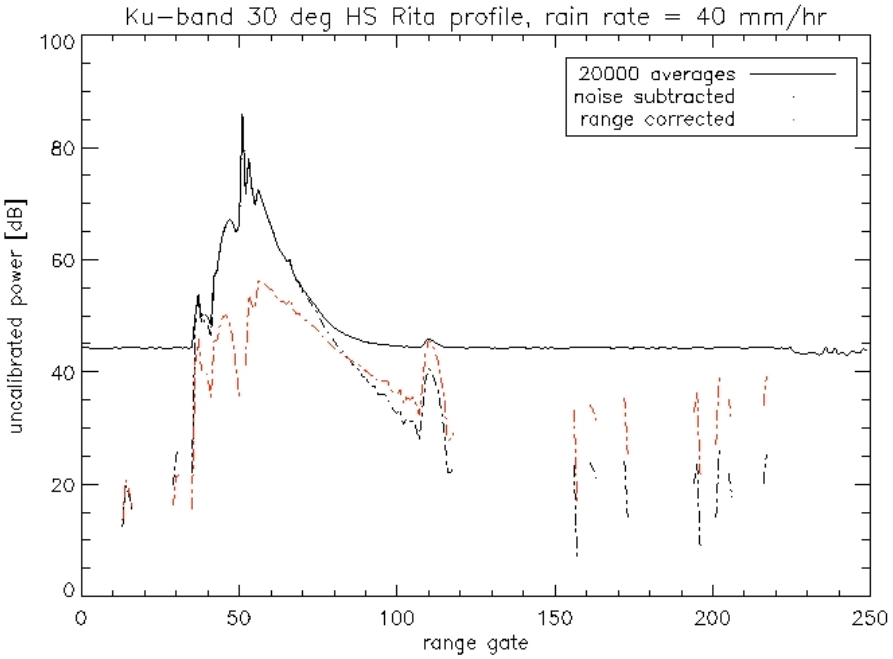

Figure 5.9. Hurricane Felix single profile at 40 mm rain rate shown with 20,000 averages, noise removal, and range correction.

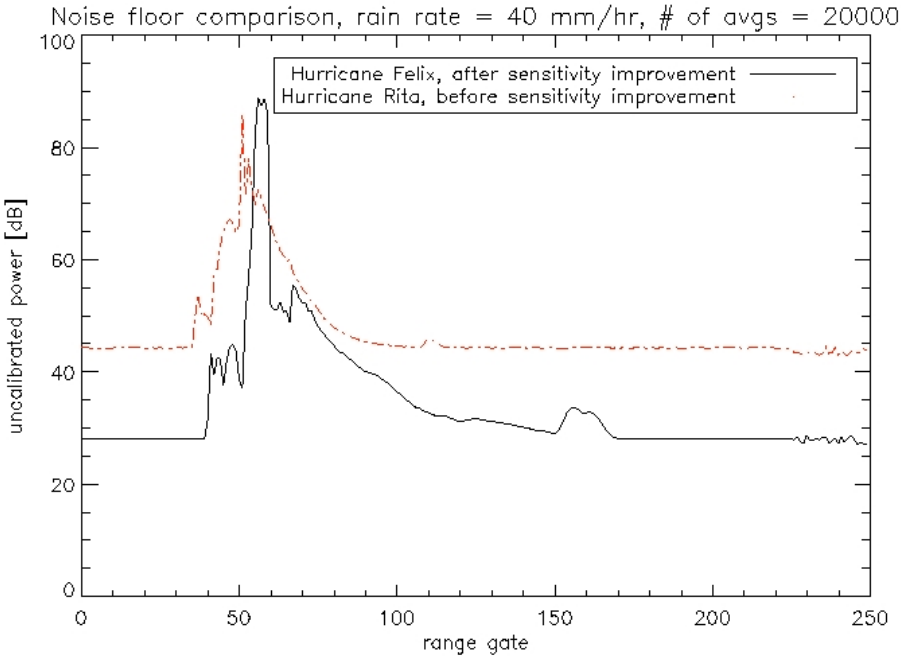

Figure 5.10. Ku-band 30 deg, Comparison of Hurricane Rita and Felix 20000 averaged profile noise floor.

5.5 Hurricane Felix Spectral Processing Preliminary Results:

Spectral processing is useful since it can show the full Doppler spectrum rather just an estimate of the spectral moments using the pulse pair algorithm. Pulse pair algorithm assumes a Gaussian distribution for the Doppler spectrum and estimates the first three moments of the Doppler spectrum. Doppler spectrum is not always Gaussian shaped. There are occasions when it contains two components to the Doppler spectrum representing a bimodal distribution rather than Gaussian. This results in inaccurate estimation of backscatter power when pulse pair technique is employed. Spectral processing helps with separating the contributions from two sources of backscatter from both ocean surface return and volumn backscatter.

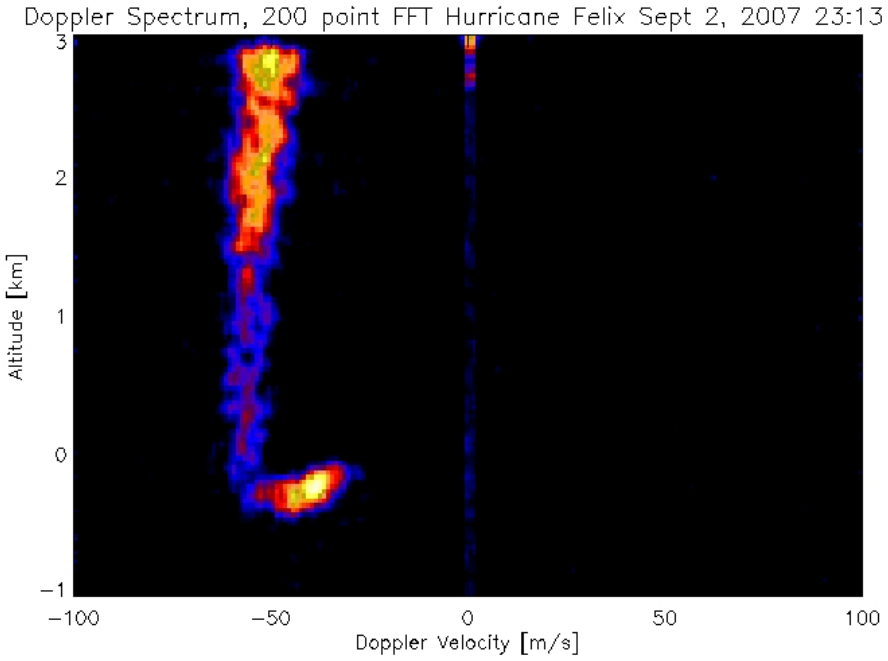

Figure 5.11. Ku-band 30 deg, FFT of 200 profiles.

The Ku-band's 30 degrees incidence angle will be used in this section for spectral processing. Range gates that are close to the ocean surface will contain contributions from both the stationary ocean surface and the more turbulent rain filled atmosphere

at slant incidence angles. The Doppler spectrum for those range gates will be composed of two components of two different Doppler frequencies. Figure 5.11 shows the Doppler spectrum for all range gates, it was obtained by taking the Fast Fourier Transform (FFT) of 200 consecutive profiles. The bright vertical line represents the volume return from precipitation. The big bright region in the lower part of the graph represents the ocean surface return.

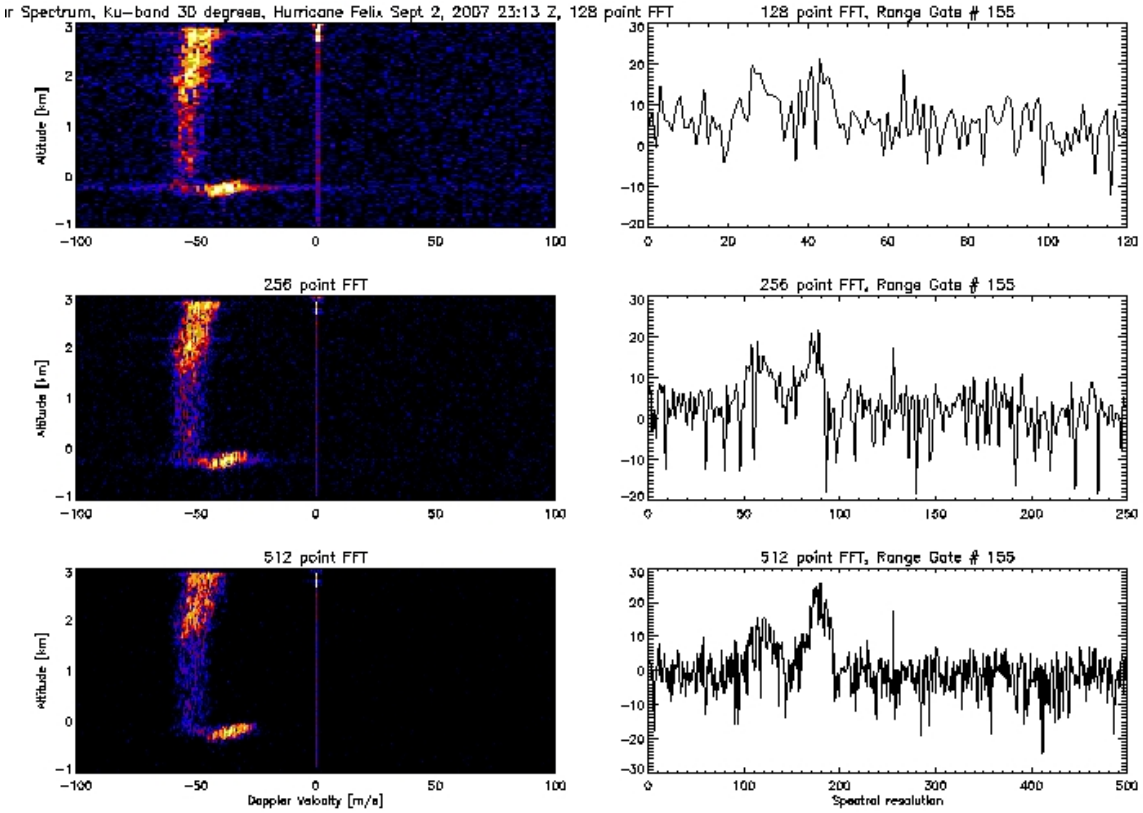

Figure 5.12. Ku-band 30 deg, FFT with 128, 256, and 512 points, showing ocean surface and volumn contamination range gate number 155.

When computing the FFT, it is more efficient to use a number of points that is a multiple of two. Figure 5.12 shows different number of points multiples of two used when computing FFT. 128 point FFT appears to have low spectral resolution, where 512 point FFT has higher resolution. However higher number of points used translates to more noise.

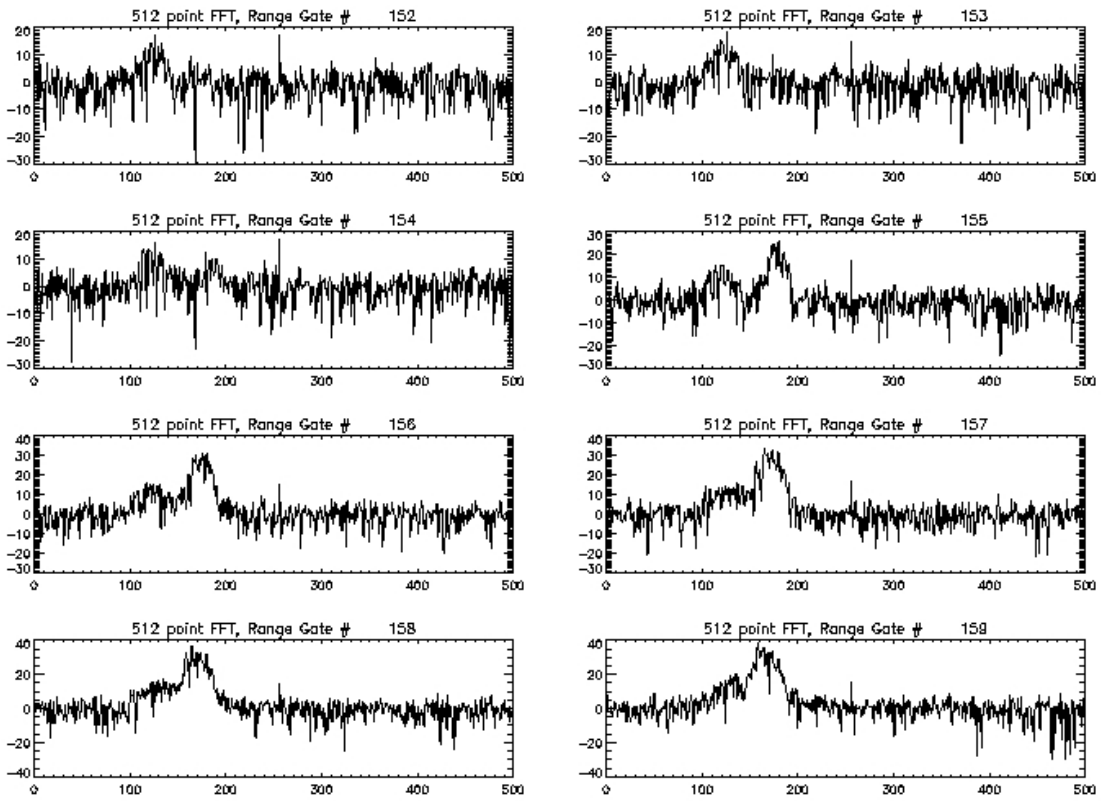

Figure 5.13. Ku-band 30 deg, 512 point FFT of range gates of the contaminated range gates close to the ocean surface.

Figure 5.13 shows 512 point FFT over eight range gates close to the ocean surface. One can see the disappearance of the volume backscatter and the emergence of the surface backscatter as range gate progresses closer to the ocean surface. Similar plots were made using 128 point FFT and 256 FFT. It is clear that using 512 point FFT the two contributions can be separated.

It was shown in this section in one particular example of raw data that the contribution of from the ocean surface and atmospheric backscatter and be individually identified. Given that the two components are found, the question becomes how is it possible to distinguish between the two contributions. It can be seen in Figure 5.13 that both contributions vary in amplitude as a function of distance to ocean surface. Moreover, due to the azimuthal rotation of the antenna, the atmospheric backscatter

goes from positive to negative Doppler frequency, with the ocean surface backscatter lagging in frequency. There are times where the two contributions are completely embedded within each other. More work need to be done in terms finding the fitting algorithm to remove one contribution from another.

CHAPTER 6

CONCLUSION

6.1 Summary of Work Completed

This thesis described the system improvements made from 2005 to 2007 on IWRAP. IWRAP sensitivity was improved by means of modifying the Ku-band system front-end. This was achieved by obtaining a new LNA with improved noise figure, and also by reconfiguring the front-end in a more efficient setup such that the loss between the antenna and the LNA is minimized, this was made possible by a dual rotary joint such that the front-end can be placed on the antenna. As a result, the overall system noise figure is improved by more than 7 dB. With the new front-end configuration, there was a problem of calibration pulse fluctuation due to the fundamental limitation of the dual port rotary joint, the problem is diagnosed and mitigated by combination of relocating components and rewiring the power lines, and the installation of microwave absorbers. As a result, the fluctuation is contained to a acceptable level and it is characterizable due to its rotational dependence.

A raw data acquisition system Pentek 7631 was implemented in 2005. Due to the shear size of the raw data volume, an effective data processing method, a software based pulse pair algorithm was developed. Data can now be processed to store accumulated sum of raw power and covariance. To ensure successful radar operation, Real time display software was developed in the form of power range gate plot for each of the four radar channels and also a PPI display showing reflexivity equivalent and Doppler. A new encoder acquiring the antenna position data was also implemented and successfully tested providing us more precision when recording antenna positions.

With the data collected in multiple experiments, we were able to verify these hardware improvements. We showed selected measurements in Hurricane Rita and Felix including eye wall penetration during maximum winds. Winter 2006 experiment we were able to validate ASCAT measurements by modifying IWRAP to transmit 60 degree incident angle at C-band. High wind model function is being developed. Data collected after Ku-band improvement does show the ability to profile further into the atmosphere potentially expand the region of data sets where two frequency method can be applied. Finally, with raw data, we have the potential of separating the echo from ocean and atmosphere. Using FFT, we are able to see the contributions from the two constituents in data at close range to the ocean surface.

6.2 Future Work

It has been shown that it is possible to separate contributions from ocean surface and volume using raw data. It is hypothesized that efficient spectral signal processing algorithms can be implemented in real time or near real time. We will investigate signal processing approaches and wind retrieval methods to derive wind and reflectivity fields from data collected by IWRAP. A more automated spectral signal processing algorithm must be implemented to prove its working in real time. And comparison with other measurements such as drop sonde to verify the algorithm is working. Once completed, it is possible to derive atmospheric wind all the way down to the ocean surface.

Ku-band front-end upgrade should be revisited in order for calibration pulse fluctuation level to be less than 1 percent. Rotary joint isolation issue must be resolved. It is necessary to increase isolation between the two channels or put more gain on the antenna however may not be the most elegant solution. Although there was sensitivity improvement in Ku-band measurement, its not enough in order to penetrate all the wall down to the surface. Other method such as implementing pulse compres-

sion should be investigated. For future UAV based instruments, pulse compression is required due to the high altitude. IWRAP could be a proof of concept for such a project.

New dual-polarized antenna with better gain and cross-polarization ratio would allow retrieval of C- and Ku-band, H- and V-pol profiles from precipitation. With this capability at different incidence angles, it is possible to investigate best possible scenario setup for measurement of precipitation and for ocean surface backscatter under extreme conditions. By looking at the different polarization, band, and incident angles, the results could prove of importance for future spaceborne instrument designed for studying ocean surface vector wind and tropical cyclones.

With enough sensitivity to profile down to the ocean surface and the ability to separate contribution from both the surface echo and the volume echo, benefit of such a system is enormous. The attenuation from rain would be better understood, and more complete atmospheric as well as ocean surface wind measurements are possible.

APPENDIX A

DOPPLER SPECTRUM OF CONTAMINATED RANGE GATES

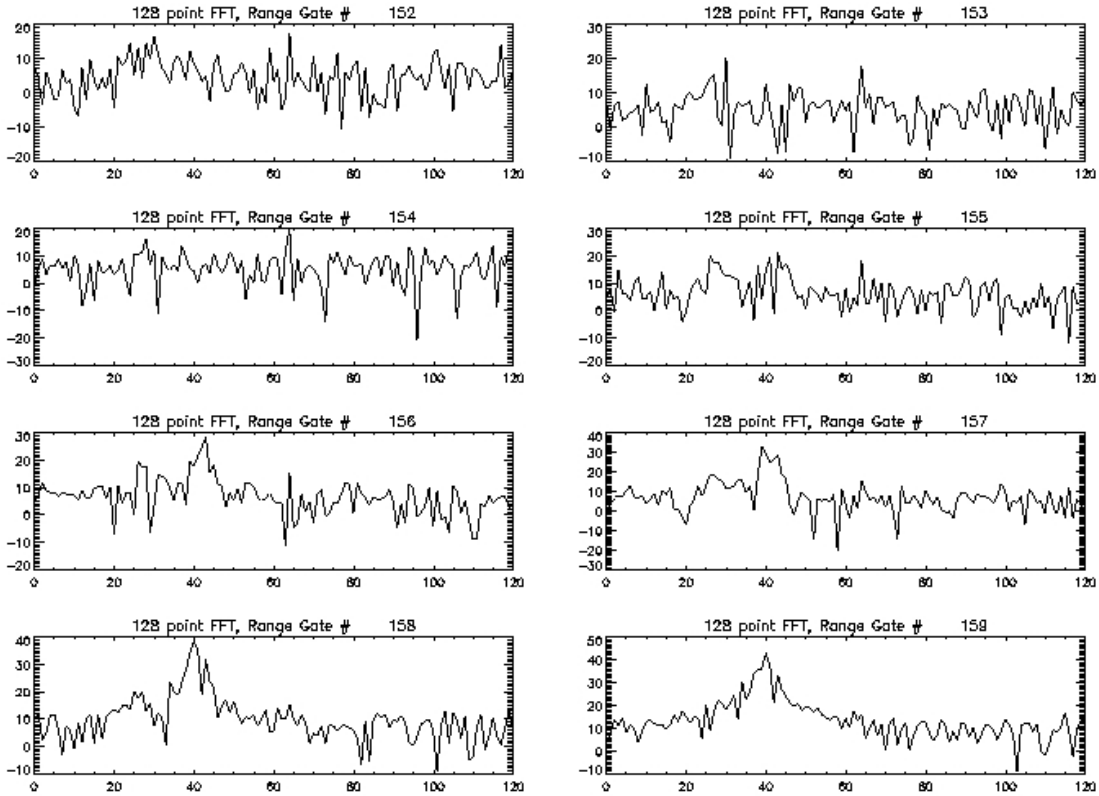

Figure A.1. Ku-band 30 deg, 128 point FFT of range gates of the contaminated range gates close to the ocean surface.

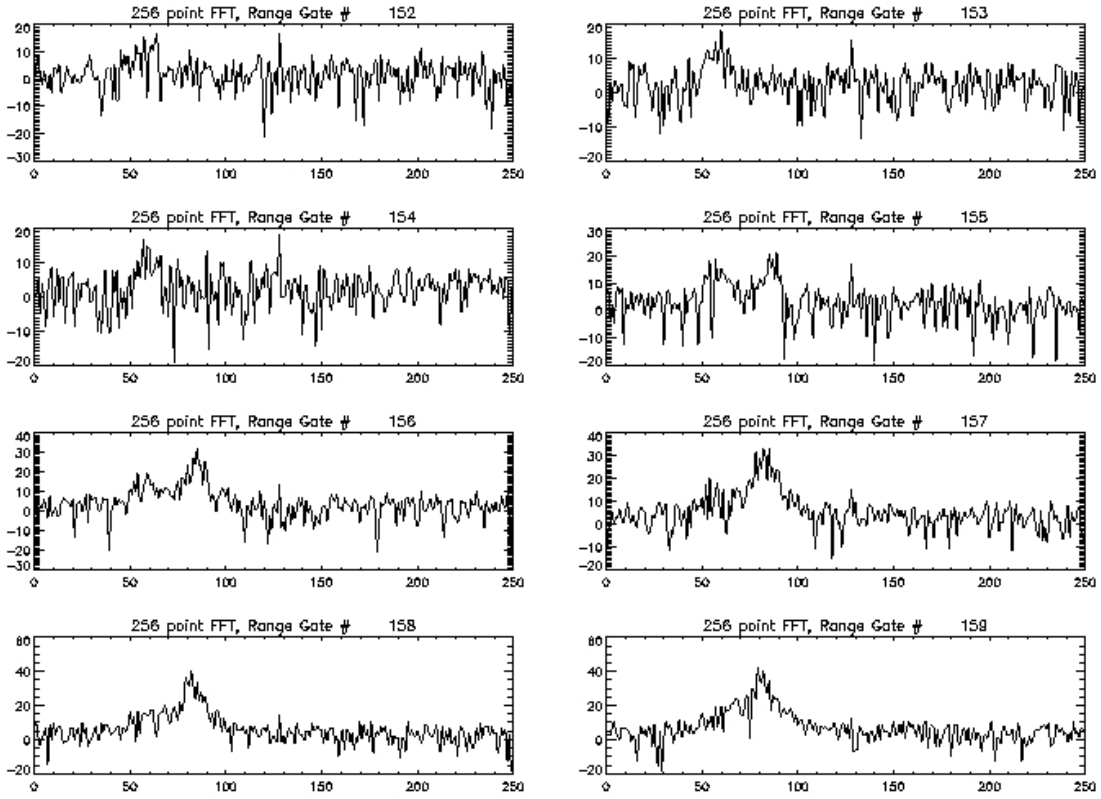

Figure A.2. Ku-band 30 deg, 256 point FFT of range gates of the contaminated range gates close to the ocean surface.

APPENDIX B

DATA STRUCTURE AND PRODUCTS

The Pentek output of raw data structure is shown in Table B.1. Using the pulse pair algorithm described in Chapter 4.2, the data volume is significantly reduced. moreover, the pulse pair data structure, Table B.2, is not the same as that of the raw data, keeping only the encoder information, and navigation data, processes I and Q, deriving power and covariance, which is one step closer of deriving sigma0 and Doppler velocity. Figure B.1 shows a flow chart of data and possible products generated by IWRAP. Fast Fourier Transform (FFT) can be performed on the raw data allowing the capability of spectral processing. Navigation data from the NOAA P3 data stream is appended in IWRAP raw data, useful in flight information such as latitude, longitude, time; behavior of the aircraft such as airspeed, altitude, roll, pitch, and yaw; in flight measurements such as in flight wind speed, but most importantly the SFMR, or Stepped Frequency Microwave Radiometer provide wind speed and rain rate. SFMR information is crucial component of IWRAP data set because it measures the integrated rain rate of the entire sampled volumn which serves as validation for IWRAP measurements. Navigation data structure is show in Table B.3.

Element Name	Definition	Size [bytes]
header	"HEADER!"	8
hdct	Number of "HEADER!" counted	4
status	-	4
timehi	UTC time part 1/2	4
timelo	UTC time part 2/2	4
lengthi	Length of in phase part of the signal or I	4
ichan	In phase for 4 PRF cycles	2048
lengthq	Length of quadrature part of the signal or Q	4
qchan	Quadrature for 4 PRF cycles	2048
encodc	C-band antenna azimuthal position data	2
encodku	Ku-band antenna azimuthal position data	2
nav	1 Hz navigation data total of 34 parameters	136
PACKET SIZE	Total size of each raw data packet	4268

Table B.1. Raw data packet format

Element Name	Definition	Size [bytes]
hdct	Number of "HEADER!" counted	4
timehi	Part 1 of UTC time	4
timelo	Part 2 of UTC time	4
pwr	Accumulated power for 250 range gates	500
cov	Accumulated covariance for 250 range gates	500
encodc	C-band antenna azimuthal position data	2
encodku	Ku-band antenna azimuthal position data	2
nav	1 Hz navigation data total of 34 parameters	136
PACKET SIZE	Total size of each pulse pair packet	1152

Table B.2. Pulse pair data packet format

Element Name	Definition	Size [bytes]
1. DATE	UTC date	4
2. TIME	UTC time	4
3. SLA	Latitude	4
4. SLO	Longitude	4
5. SGY	Aircraft velocity North (m/s)	4
6. SGX	Aircraft velocity East (m/s)	4
7. SVS	Aircraft velocity Vertical (m/s)	4
8. SDA	Drift angle	4
9. SHD	Heading	4
10. SPC	Pitch	4
11. SRL	Roll	4
12. TK	Track	4
13. GS	Ground speed (m/s)	4
14. TSM	True air speed (m/s)	4
15. RA	Radar altitude (m)	4
16. WD	Flight level wind direction	4
17. WS	Flight level wind speed	4
18. WZ	Flight level wind speed vertical	4
19. TA	Flight level temperature	4
20. RD	Downlooking radiometer in celsius	4
21. RS	Sidelooking radiometer in celsius	4
22. TD	Dewpoint temperature	4
23. RH	Relative humidity (percent)	4
24. SP	Surface pressure (mmb)	4
25. PS	Selected pressure either PS1 or PS2	4
26. BT1	AXBT channel in celsius	4
27. BT2	-	4
28. BT3	-	4
29. SFWS	AOC SFMR windspeed	4
30. SFRR	AOC SFMR rain rate	4
31. SFDV	AOC SFMR error flags	4
32. SFWSM	Umass SFMR windspeed	4
33. SFRRM	Umass SFMR rain rate	4
34. SFDVM	Umass SFMR error flags	4
PACKET SIZE	Total size of each navigation packet	136

Table B.3. Aircraft navigation data packet format

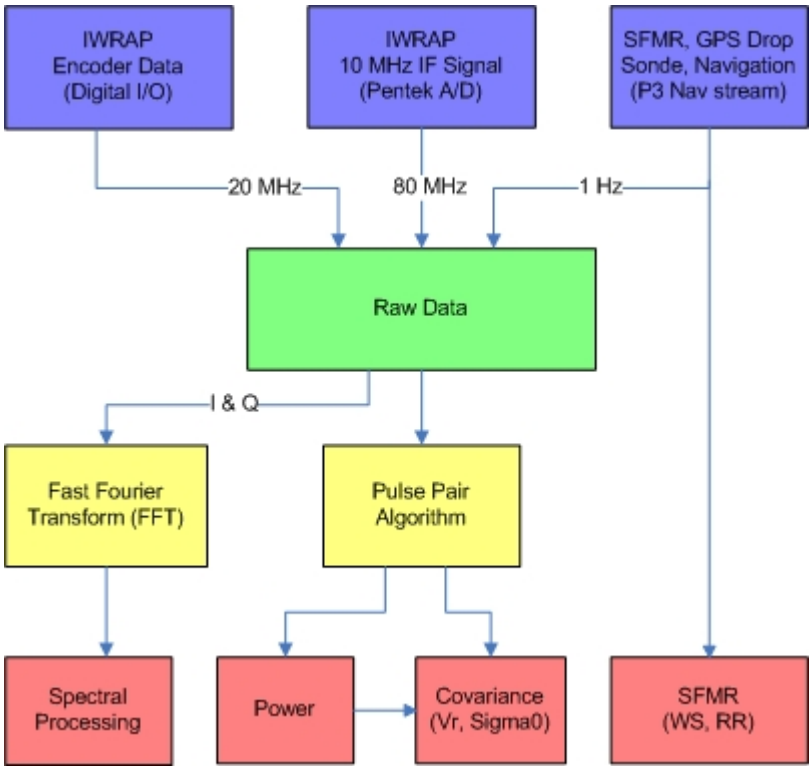

Figure B.1. IWRAP data processing and product flow chart.

BIBLIOGRAPHY

[1] Ad Stoffelen, Marcos Portabella. On bayesian scatterometer wind inversion. *IEEE Transactions on Geoscience and Remote Sensing 44* (June 2006), 1523–1533.

[2] Castells, Antoni. Design and implementation of the imaging wind and rain airborne profiler. Master's thesis, University of Massachusetts at Amherst, 2001.

[3] Christopher C. Hennon, David G. Long, Frank J. Wentz. Validation of quikscat wind retrievals in tropical cyclone environments. *IEEE Transaction*.

[4] Daniel Esteban Fernandez, Xuehu Zhang, Antonio Castells David McLaughlin James Carswell Paul Chang Laurence Connor Peter Black Frank Marks. The imaging wind and rain airborne profiler- a dual frequency dual polarized connically scanning airborne profiler radar. *0-7803-7929-2/03IEEE* (February 2003), 4246–4248.

[5] Doviak, R. J., Zrnic D. S. *Doppler Radar and Weather Observations*. Academic Press, San Diego, California, 1984.

[6] Fawwaz T. Ulaby, Richard K. Moore, Adrian K. Fung. *Microwave Remote Sensing Active and Passive Volume II*. Artech House, Norwood, Massachusetts, 1982.

[7] Fernandez, Daniel Esteban. *Remote Sensing of the Ocean and the Atmospheric Boundary Layer within Tropical Cyclones*. PhD thesis, University of Massachusetts at Amherst, February 2005.

[8] Freilich, M.H. Seawinds algorithm theoretical basis document.

[9] James R. Carswell, Steven C. Carson, Robert E. McIntosh Fuk K. Li Gregory Neumann David J. Mclaughlin John C. Wilkerson Peter G. Black S. V. Nghiem. Airborne scatterometers: Investigating ocean backscatter under low- and high-wind conditions. *Procedings of the IEEE* (December 1994), 1835–1860.

[10] Pozar, David M. *Microwave and RF Design of Wireless Systems*. John Wiley and Sons, Inc, Danvers, Massachusetts, 2001.

[11] William J. Plant, Eugene A. Terray, Robert A. Petitt Jr William C. Keller. The dependence of microwave backscatter from the sea on illuminated area: Correlation times and lengths. *Journal of Geophysical Research 99* (May 1994), 9705–9723.